Chair of Materials Physics

Master's Thesis

In-situ thermo-mechanical cycling of Si-TiW-Cu thin film structures

Benjamin Seligmann, BSc

May 2022

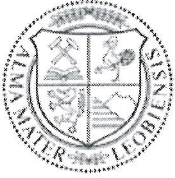

MONTANUNIVERSITÄT LEOBEN
www.unileoben.ac.at

EIDESSTATTLICHE ERKLÄRUNG

Ich erkläre an Eides statt, dass ich diese Arbeit selbständig verfasst, andere als die angegebenen Quellen und Hilfsmittel nicht benutzt, und mich auch sonst keiner unerlaubten Hilfsmittel bedient habe.

Ich erkläre, dass ich die Richtlinien des Senats der Montanuniversität Leoben zu "Gute wissenschaftliche Praxis" gelesen, verstanden und befolgt habe.

Weiters erkläre ich, dass die elektronische und gedruckte Version der eingereichten wissenschaftlichen Abschlussarbeit formal und inhaltlich identisch sind.

Datum 23.05.2022

____
Unterschrift Verfasser/in
Benjamin Seligmann

Acknowledgment

Before diving into this thesis, I would like to thank a couple of persons, who contributed immensely to this work. Alexander Jelinek saved me a lot of time by precutting the samples. The in-situ experiments were conducted by Markus Alfreider and Michael Wurmshuber who also helped together with Michael Burtscher with EBSD scanning. During the experimental process the guidance combined with the open mindedness towards my proposals by Daniel Kiener were highly appreciated. Special thanks to Markus Alfreider, who was always available for questions and assisted with advice and support. Last but not least I want to thank my parents, Hanne and Stefan, as without their support up to this point this thesis would not have been possible.

Abstract

Material systems in microelectronic devices are often combining many layers of different materials. Increased heating and cooling rates due to higher working frequencies of integrated circuits cause higher loads on the devices. This may lead to delamination of thin films and/or thermo-mechanical fatigue depending on internal stress states.
The present work investigates these internal stress and strain states by performing in-situ thermal cycling experiments on a Si-TiW-Cu material stack. The Cu layer experiences significant plastic deformation at higher temperatures ($T_{max} = 400\,°\mathrm{C}$) causing void formation at grain boundaries and the TiW-Cu interface. However the load is not high enough to cause visible crack growth or delamination, even in pre-notched samples and in samples with a chemically modified TiW interface. The lack of failure can be linked to insufficient internal stresses and strain rates.
To improve the workflow a semi-automatic image processing program is successfully implemented. It enables faster and more accurate measurements of the curvature of the Si-TiW interface.
An analytical model is proposed to calculate internal elastic and plastic stresses and strains in three layers. A FEA analysis is conducted to validate this model, which can predict the region of plastic deformation in the Cu phase.
The presented experimental setup combined with the analytical model promises a greater understanding of fatigue and damage processes in thin film compounds of arbitrary layer count and material composition.

Contents

List of Symbols . . . xii

List of Figures . . . xvii

List of Tables . . . xviii

1. Introduction **1**

2. Theory **3**

2.1. Thin film materials . . . 3

2.2. Thermo-mechanical fatigue . . . 5

2.3. Material . . . 6

2.4. Modelling intrinsic stresses . . . 7

2.4.1. Preliminary work . . . 7

2.4.2. Elastic response . . . 9

2.4.3. Plastic response . . . 11

3. Experimental methods **13**

3.1. Sample preparation . . . 13

3.2. Heating and EBSD measurement . . . 14

3.3. Image processing . . . 16

3.4. Finite element analysis . . . 18

4. Results **20**

4.1. Beam curvature . . . 20

4.2. Internal stress distributions . . . 22

4.3. Microstructural changes . . . 26

5. Discussion **32**

5.1. Image processing . . . 32

5.2. Experimental setup . . . 35

5.3. Thermo-mechanical fatigue . . . 36

5.3.1. Microstructural changes . . . 36

5.3.2. Curvature measurements . . . 40

5.3.3. Modelling of internal stresses 42
5.3.4. Delamination 46

6. Conclusion **51**

Appendix A. Alternate experimental setup **53**

Appendix B. Internal stress plots **55**

List of Symbols

α Coefficient of Thermal Expansion

ΔG Free energy needed for void formation

ϵ Strain

γ_i Interfacial energy

κ Curvature

ν Poisson's ratio

σ Stress

σ_h Historic accumulated residual stress due to plastification

σ_r Residual stress

σ_y Yield strength

τ Shear stress

τ_p Peierl's-stress

$_{s,i}$ Subscripts for substrate and respective layers of film

a, b Geometric dimensions

b Burger's vector

c Uniform strain (Hsueh elastic model)

d Distance between crystal planes

E Young's modulus

$EBSD$ Electron Backscatter Diffraction

F Geometric factor

f_v Geometric factor

fcc face centered cubic

FEA Finite Element Analysis

FIB Focused Ion Beam

G Shear modulus

H Bilinear plastic modulus

h_b Bending axis (Hsueh elastic model)

HT High temperature

I Moment of Inertia

J J-Integral

K Stress intensity factor

LCF Low Cycle Fatigue

M Bending moment

ORB Oriented fast and Rotated Brief, keypoint detector

$PEEQ$ Equivalent plastic strain

r Radius

R^2 Coefficient of determination

RT Room Temperature

SEM Scanning Electron Microscope

T Temperature

t Layer thickness

UTS Ultimate Tensile Strength

VB Samples experiencing vacuum break in production

x, y, h Coordinates

List of Figures

2.1. 5

2.2. Sketch of a freestanding beam according to linear beam theory. 8

2.3. Stress and strain trends in a bent beam. Blue (dash-dotted) shows the continuous strains in the beam, and orange (long dashes) depicts stresses. Short dashes in black show the single layers of the material architecture. In (b) the black dotted line shows the elastic-plastic transition. 10

2.4. Sketch of a bilinear stress-strain curve. H depicts the plastic modulus. The dashed line shows an idealized perfectly plastic response. 11

3.1. Example of a sample with notch, slightly tilted at 1000x magnification. The bottom of the beam is the Si layer, followed by TiW and Cu. . . . 14

3.2. Exemplary Heating Cycle. 15

3.3. The working process of the semi-automated curvature detection program. In (a) the original image can be seen. The process consists of a Canny edge detection step (b), followed by masking (c) and conversion to binary (d). Finally a connecting composites algorithm leaves only edges belonging to the interface. The scale bar in (a) is representative for all figures. 16

3.4. Exemplary image of a FEA model. From bottom to top one can see the Si wafer, the TiW diffusion layer and the Cu metallization. 18

4.1. Curvature values from experiment and FEA in $^{10^{-4}}/_{\mu m}$. For comparison the elastic model of Hsueh is shown as a black line. 21

4.2. 22

4.3. Stress distribution using the analytical model at room temperature after three cycles using experimental data from CuTiW-VB-Notch (a) and the FEA model for CuTiW-VB-Notch (b). Negative stresses depict compressive stresses. The interfaces are depicted by dashed black lines. The dash dotted lines divide the elastic (I) region, the region plastically deformed below maximum residual stress (II) and the region deformed to maximum residual stress (III). 24

4.4. The tip of a notched sample. From bottom to top Si (white), TiW (shaded grey) and Cu (shaded orange) is shown. 25

4.5. SEM overviews of the post experiment samples at 1000x magnification. Samples CuTiW (a), CuTiW-Notch (b), CuTiW-VB (c) and CuTiW-VB-Notch (d). 27

4.6. Band Contrast Maps acquired by EBSD before (a) and after (b) the experiment. From top to bottom it is CuTiW-Notch around the notch area, CuTiW-VB, CuTiW-VB-Notch, CuTiW-VB-Notch around the notch area. The image width is in the magnitude of 10-15 µm. 28

4.7. Before (a) and after (b) heating inverse pole figure maps from sample CuTiW-VB-Notch around the notch area. (c) shows the inverse pole legend. 28

4.8. Examples for void formation. (a) (front view) and (b) (top view) are sections from CuTiW-VB at 7000x and 10000x magnification respectively and (c) is a top view of sample CuTiW-VB-Notch at 7000x magnification. Arrows point at voids at grain boundaries and the rectangular dashed regions show cleavage between redeposited material and original Cu layer. 29

4.9. Examples for rounding of grain boundaries on Cu surface. Top view images of CuTiW-Notch ((a) and (b)) at 7000x magnification and CuTiW-VB ((c) and (d)) at 5000x and 12000x magnification respectively. Arrows indicate void formation at grain boundaries. 30

4.10. Material flow inside the notch. CuTiW-Notch (a) and CuTiW-VB-Notch (b) at 7000x and 15000x magnification respectively. 31

4.11. Examples for material extrusions at the Si-TiW interface. Samples CuTiW-Notch (a) and CuTiW-VB-Notch (b) at 7000x and CuTiW-VB (c) at 3000x magnification. Arrows point towards these material extrusions. 31

5.1. Comparison of possible curvature measurement techniques. (a) shows the measured curvature values as well as linear fits. (b) shows the sum of the least squares yielded by fitting. . . . 33
5.2. Void growth stages. Sample CuTiW-VB preheating (a) at 7000x and after cycle two (b) and cycle three (c) at 10000x magnification respectively. Larger pores (arrow) seem to stay at their size between cycle two and three while smaller ones (dotted circles) continue growing. . . 38
5.3. Detail image (12000x magnification) of small pore formation and sliding grain boundaries. On the top of sample CuTiW-VB it can be seen that the amount and size of the pores depends on the microstructure below (maximum in detail a). Detail b shows an example of sliding grain boundaries. . . . 40
5.4. Redeposition (dashed rectangles) during EBSD area preparation on CuTiW-VB-Notch, (a) and (b), and CuTiW-Notch (c). All images are taken at 7000x magnification. The bottom of (a) shows the backside of the beam. . . . 41
5.5. Unfinished sample preparation of the backside (CuTiW-Notch). Both images taken with 7000x magnification. . . . 42
5.6. Analytical model of CuTiW-VB-Notch. Rows correspond to the cycles and columns to low temperature and maximum temperature. In (h) the total accumulated plastic strain after all cycles is shown. The dash dotted lines divide the elastic (top) region, the region plastically deformed below maximum residual stress (middle) and the region deformed to maximum residual stress (bottom) in case of the low temperatures, in case of high temperatures it divides elastic (top) and plastic (bottom) regions. . . . 44
5.7. FEA model of CuTiW-VB-Notch. Rows correspond to the cycles and columns to low temperature and maximum temperature. In (h) the total accumulated plastic strain after all cycles is shown. The dash dotted lines divide the elastic (top) region, the region plastically deformed below maximum residual stress (middle) and the region deformed to maximum residual stress (bottom) in case of the low temperatures, in case of high temperatures it divides elastic (top) and plastic (bottom) regions. . . . 45
5.8. The accumulated equivalent plastic strain PEEQ in CuTiW-VB-Notch. The corresponding color legend is shown in figure 5.9. (a) to (g) show the area around the notch during cycling, (h) shows the entire beam. . 48

5.9. Legend for figure 5.8. 49

A.1. Proposal of simultaneous bi- and trilayer experiment 53

B.1. Analytical model of CuTiW. Rows correspond to the cycles and columns to low temperature and maximum temperature. In (h) the total accumulated plastic strain after all cycles is shown. The dash dotted lines divide the elastic (top) region, the region plastically deformed below maximum residual stress (middle) and the region deformed to maximum residual stress (bottom) in case of the low temperatures, in case of high temperatures it divides elastic (top) and plastic (bottom) regions. 56

B.2. FEA model of CuTiW. Rows correspond to the cycles and columns to low temperature and maximum temperature. In (h) the total accumulated plastic strain after all cycles is shown. The dash dotted lines divide the elastic (top) region, the region plastically deformed below maximum residual stress (middle) and the region deformed to maximum residual stress (bottom) in case of the low temperatures, in case of high temperatures it divides elastic (top) and plastic (bottom) regions. 57

B.3. Analytical model of CuTiW-Notch. Rows correspond to the cycles and columns to low temperature and maximum temperature. In (h) the total accumulated plastic strain after all cycles is shown. The dash dotted lines divide the elastic (top) region, the region plastically deformed below maximum residual stress (middle) and the region deformed to maximum residual stress (bottom) in case of the low temperatures, in case of high temperatures it divides elastic (top) and plastic (bottom) regions. 58

B.4. FEA model of CuTiW-Notch. Rows correspond to the cycles and columns to low temperature and maximum temperature. In (h) the total accumulated plastic strain after all cycles is shown. The dash dotted lines divide the elastic (top) region, the region plastically deformed below maximum residual stress (middle) and the region deformed to maximum residual stress (bottom) in case of the low temperatures, in case of high temperatures it divides elastic (top) and plastic (bottom) regions. 59

B.5. FEA model of CuTiW-VB. Rows correspond to the cycles and columns to low temperature and maximum temperature. In (h) the total accumulated plastic strain after all cycles is shown. The dash dotted lines divide the elastic (top) region, the region plastically deformed below maximum residual stress (middle) and the region deformed to maximum residual stress (bottom) in case of the low temperatures, in case of high temperatures it divides elastic (top) and plastic (bottom) regions. 60

List of Tables

3.1. Geometries of the prepared samples. VB stands for vacuum break. . . . 13
3.2. Mechanical properties of the layers. 19

4.1. Maximum temperatures reached in each cycle. 20
4.2. K_{II} values during experiment. RT stands for room temperature and HT for high temperature 25

1. Introduction

The world around us is technologically advancing faster than ever. Especially in the sector of microelectronics this progress is significant, as many other sectors are dependent on this field. Microchips and processors are not only used in computers, but essentially in many every day used items. From cars and their keys to smart watches and mobile phones. In 1965 Gordon Moore postulated, that the number of transistors in an integrated circuit would be doubling every year [1]. Later he revised his statement to doubling every two years [2]. Nonetheless, this almost 50-year evolution has led to absurd numbers of transistors in microchips.

Simultaneously the trend for technical devices has pointed to smaller and thinner geometries. Thermal management and microchip architecture are therefore of utmost importance today. The reduction in space requires thinner transistors, where the mechanical responses of the partly highly complex material combinations can deviate from macroscopic observations.

Secondly, thermal fatigue is all the more threatening the functionality of all microelectronic parts as increasing frequencies in microchips lead to higher heating and cooling rates. It is vital to understand these fatigue mechanisms to ensure the structural integrity and especially the functionality at as long as possible lifetime of the device.

Thus, the present work focuses on an in-situ experiment with samples size in the micrometer range, where the known behaviour of thermostatic bimetallic strips is exploited. Combining two or more layers with different coefficients of thermal expansion leads to bending of the strip, as the connection between them constrains the linear expansion. Observing the curvature at a given temperature reveals the stress and strain state in the specific layers.

This information can be used to predict critical stresses which would cause delamination, as well as observe the elastic-plastic strain response, which depends on the materials used. In the present case a common microelectronic material combination including Si, TiW and Cu is tested [3–8].

In the following chapters, the fundamental theory behind thermal fatigue and thin films is presented. Furthermore, the experimental methods are laid out, after which results and discussion of these are shown. This includes also in-situ Scanning Electron

Microscopy (SEM) images observing fatigue phenomena.
The experiment is enhanced by a semi-automatic computer vision workflow to determine the curvature values. In the end an improved experimental set up is introduced which uses the proposed adaptation of an analytical stress-strain model for plastic response in three thin film layers. This model is compared to a Finite Element Analysis (FEA) for validation.

2. Theory

The following chapter gives an overview about properties of thin film material systems regarding architecture and curvature due to internal stresses like thermal and residual stresses. It also addresses fatigue mechanisms during repeated thermo-mechanical loading.

2.1. Thin film materials

This section addresses important factors about layered materials in general, especially the origin of internal stresses resulting in curvature changes.
A thin film system consists of two main parts, the substrate and the film. In the special case of microelectronics, the substrate is often Si or any other semiconductor, frequently in the form of a wafer [3–6]. The film includes one or more layers of different or even the same materials as the substrate, depending on the desired functionality. These layers are deposited via various processes, for example physical or chemical vapor deposition. As many materials are combined in layered structures it is quite obvious that not only functionality but also the mechanical properties of these systems are of utmost importance. Failing connections between materials induce a reduced functionality, which often leads to increased energy dissipation as heat resulting in an increase in power consumption and/or a decrease in operating speed over time.
This thesis will therefore investigate the mechanical properties of a particular interface between a Cu and a TiW layer in a multilayer thin film. The specific architecture of the system is described in chapter 2.3. For the moment, the focus lies on the mechanical challenges an interface is confronted with.
Discontinuations are often spots of mechanical weakness. In conventional 'homogeneous' materials this can include pores or incoherent precipitates within the matrix [9]. Also surfaces and especially surface imperfections are prone to be the nucleation points of mechanical failure like cracking. Layered structures magnify these problems. Interface engineering is a fast-progressing field, which tries to optimize mechanical properties, adhesion and functionality [10–13].
Delamination of layered structures in microelectronics is mainly governed by internal

loads. These include residual stresses and/or thermal loads. Residual stresses are introduced while processing the film, which consists of deposition steps and post-processing. For polycrystalline films, these stresses stem from mismatches, as material deposition takes place at various places simultaneously and growing grains touch. Depending on the substrate/film combination these already deposited islands of atoms are forced into positions they would normally not occupy. Higher temperature and larger diffusion coefficients will allow these atoms to relax and diffuse into bigger islands or even closed layers. Under the premise that the conditions are not suited for single crystal formation, grains will form when islands of atoms connect. Post-processing like subsequent annealing reduces or increases these stresses, as desired for optimal structural and functional properties. In multilayered structures it is generally assumed that later deposited layers only interact with the substrate [14]. So, the residual stresses within one layer of film are not affected by the layer deposited afterwards.

Stresses within thin film structures in general lead to a phenomenon called wafer curvature. In figure 2.1a a substrate-film combination can be seen, which is not yet connected. The film is pulled by an external force to be a little bit larger. When connecting substrate and film and removing the external force on the film, it relaxes and builds up compressive residual stresses. The whole structure deforms elastically.

This curvature can also be induced by thermal loading. As a material is heated or cooled it will change shape according to its coefficient of thermal expansion (α). Different materials usually have different α, which leads to a mismatch in expansion or contraction. When stacking these materials, the layers constrain each other from changing their shape to a stress free configuration. Therefore, internal thermal stresses are induced within the layers, leading to a stress mismatch at the interface.

Measuring the curvature of a wafer allows for calculating these stresses. The measurement of the curvature can be performed mechanically, via capacitive methods or x-ray diffraction and with optical methods like laser reflection [14, 15]. The effect of a substrate bending due to a deposited film is known since the 19th century by findings of Gore [16, 17]. At the beginning of the 20th century the curvature was linked to the stresses within the film by Stoney [18]. He derived an equation known as Stoney's equation, which is used up to today, when film thickness is small compared to substrate thickness. The experiments performed in the frame of this work use a layered structure where substrate and film thickness are roughly the same, which is one reason Stoney's equation cannot be used [19]. But the concept of relating curvature to stresses is still pursued and laid out in more detail in the sections to come.

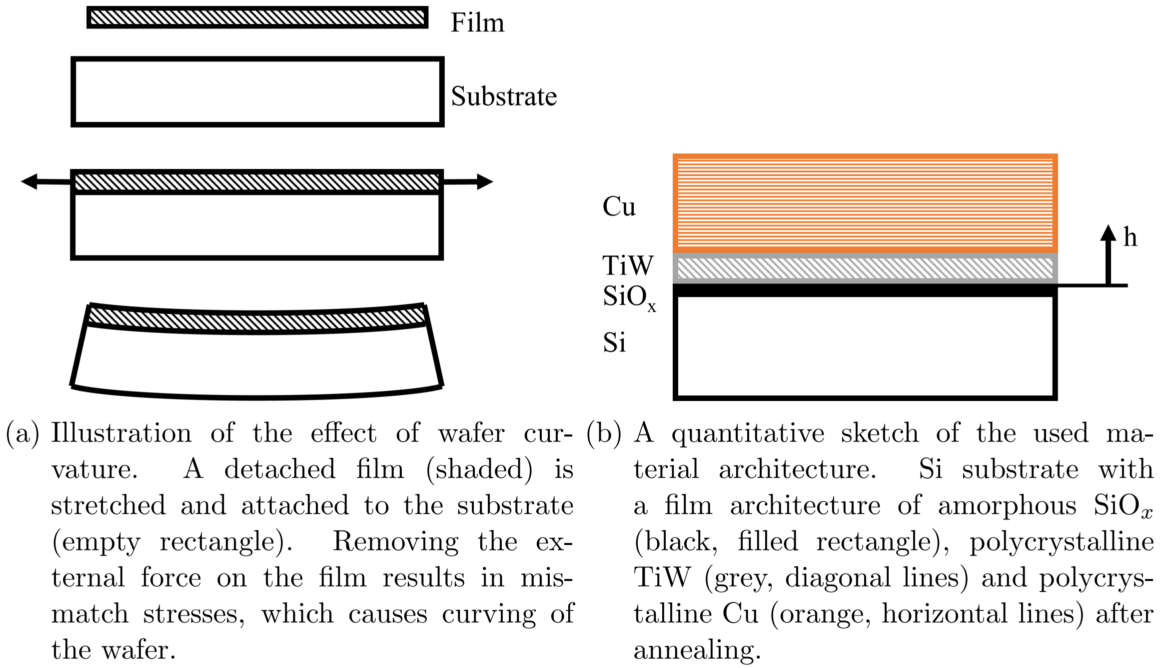

(a) Illustration of the effect of wafer curvature. A detached film (shaded) is stretched and attached to the substrate (empty rectangle). Removing the external force on the film results in mismatch stresses, which causes curving of the wafer.

(b) A quantitative sketch of the used material architecture. Si substrate with a film architecture of amorphous SiO_x (black, filled rectangle), polycrystalline TiW (grey, diagonal lines) and polycrystalline Cu (orange, horizontal lines) after annealing.

Figure 2.1.

2.2. Thermo-mechanical fatigue

It was already described that delamination must be avoided at all costs when dealing with layered systems. During its lifetime, a microelectronic device is repeatedly thermally loaded through on- and off-switching which ultimately can lead to thermo-mechanical fatigue.

Fatigue in general implies a repetitive loading of a material or workpiece below its characteristic load of failure. In the case of the present work this would be the yield strength of the weakest material in the thin film architecture. The load is induced via cyclic thermal loading. Cyclic loading leads to cyclic plasticity [20, 21]. Energy is dissipated in the material enabling defect formation and movement as the stress-strain behaviour resembles a hysteresis.

Low cycle refers to the fact that a small number of loading cycles (below 10^5 cycles) is sufficient to initiate failure. In microelectronic systems it is crucial that microstructure and interfaces stay intact as any deviation leads to a decrease in performance and an increase in power consumption or even failure of the device.

Every cycle allows for defect formation and movement. One form of defects are dislocations. They require a certain shear stress, called Peierls-stress τ_p [9], to move through a material.

$$\tau_p = \frac{2G}{1-\nu} \exp\left(-\frac{2\pi}{1-\nu}\frac{d}{b}\right) \tag{2.1}$$

G being the shear modulus and ν Poisson's ratio. The Burgers vector b and the distance between the crystal planes d govern τ_p as they contribute exponentially. For face centered cubic (fcc) materials like copper this relationship is the reason for the preferred gliding system being $\{111\}\langle 110\rangle$. τ_p is temperature dependent, as the crystal lattice gets thermally activated. Therefore, higher temperatures result in lower τ_p which is mirrored by the temperature dependent behaviour of the macroscopic yield strength.

As already described, heating and cooling a layered structure results in stresses due to restraints at the interfaces.

Combining the increasing stresses on defects and the decreasing barrier τ_p leads to defect movement at increasing temperatures. The movement of dislocations is directed by the governing shear stress and can be influenced by surfaces of any kind, for example grain boundaries, interfaces or open surfaces. An accumulation of defects can lead to pore formation and crack initiation [3]. In the examined layered structure these cracks tend to reach the interface, leading to delamination [3, 22].

In addition to dislocations, mobile defects can also include vacancies, chemical impurities and interstitial lattice atoms. They all have in common that they need to overcome an energy barrier to move through the crystal lattice.

Other possible failure mechanisms include creep and oxidation.

2.3. Material

At this point it is beneficial to point out the actual architecture of the system which is investigated in this thesis. The substrate is (001) oriented single crystalline Si, which is heated to thermally grow a 50-70 nm thick layer of SiO_x. Thereafter a 250-300 nm TiW film with about 100 nm grain size is deposited by physical vapor deposition. It experiences high compressional residual stresses after cooling to room temperature of around 1.5 GPa [23]. The deposition of TiW is followed by a seed layer of Cu. The seed film is used for easier galvanic deposition of a 5 µm thick Cu layer of approximately 2.7 µm grainsize. A schematic of this structure can be seen in figure 2.1b.

As seed and galvanic layers have different grain sizes and the Cu layer in general might have grown in preferred textures the whole wafer is exposed to a 30 min heat treatment at 400 °C. There is no significant grain growth, but the small grains of the seed layer are incorporated into the second Cu layer resulting in no obvious texture. The heat treatment prevents a later occurring uncontrollable grain growth of the electroplated Cu layer at room temperature and stabilizes the microstructure [24].

The described structure is a common material combination in the field of microelec-

tronics [3–8]. Si is the most used substrate material, SiO_x, often in the form of the stable and chemically inert SiO_2, is a suitable passivation layer. TiW is mainly used as a diffusion barrier between Si and Cu. When brought into contact, Si and Cu would diffuse into each other and build intermetallic phases which would reduce structural and especially functional capabilities of the separate layers. The top layer is Cu which is a frequently used conductor.

The deposition process is usually conducted under vacuum, but a part of this work compares the mechanical response of differently treated interfaces. In particular the interface between TiW and Cu. To achieve the biggest possible difference in response the processing under vacuum was interrupted and the wafer was exposed to air for roughly 10 min. This leads to an undefined oxide layer formation after which the Cu deposition was resumed. Samples with this treatment are called VB samples (VB standing for vacuum break).

The material combination has already been studied on several occasions [19, 25–29]. Especially the Cu layer has been investigated thoroughly regarding its mechanical properties [30–37].

2.4. Modelling intrinsic stresses

This section gives an overview regarding prior experiments as well as the mechanical equations needed to approximate internal stresses analytically.

2.4.1. Preliminary work

As this thesis is a continuation of the bachelor's thesis of Georg Kirchgaßner [38] it is only appropriate to shortly summarize his work. In a first step he roughly estimated the beam geometry disregarding the TiW layer and elastic properties of the different layers. The resulting curvature κ of the heated beam was sufficiently detectable, hence the geometry will not be changed for this work. This also allows for comparison of the results of both works. The exact geometries of the individual beams used in this thesis are listed in table 3.1.

According to linear beam theory the curvature κ of a cross sectional symmetrical beam under bending around a cross section axis is a parabola [39]. This is derived in the next equations:

$$\kappa = \frac{1}{r} = -\frac{d^2y}{dx^2} = \frac{M}{EI} \tag{2.2}$$

The corresponding radius r of κ is defined by the bending moment M as well as the

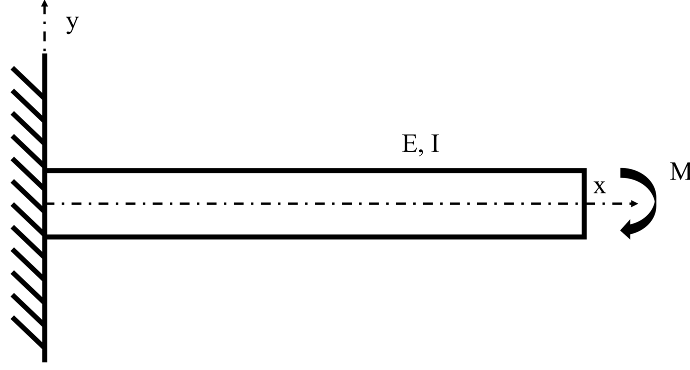

Figure 2.2.: Sketch of a freestanding beam according to linear beam theory.

average moment of inertia I and the average Young's modulus E. The axis in beam direction is x and y is perpendicular to it (compare figure 2.2). From hereon it should be pointed out that the models for this beam are always uniaxial regarding stresses and strains which allows for the use of E rather than $\frac{E}{(1-\nu)}$, as in the biaxial case of classical wafer curvature. Integrating twice reveals

$$y(x) = -\frac{M}{EI}\frac{x^2}{2} + c_1 x + c_2 \tag{2.3}$$

with

$$c_0 = -\frac{M}{2EI} \tag{2.4}$$

Using equation (2.2) to (2.4) leads to

$$-\frac{d^2y}{dx^2} = -2c_0 = \kappa \tag{2.5}$$

The curvature of the in-situ experiments can therefore be obtained by tracking an interface rich in contrast (in this case the SiO_x-TiW interface) and fitting a parabola to the acquired data points.

Kirchgaßner continued and compared several mathematical models [40–42] with the measured curvature and deflection of the beam tip with his experiments. All models are suited to predict the elastic deformation of the beam. Regarding repeated load application on the other hand, the thermal stress mismatch between the Cu and TiW layer was only correctly predicted by the tri-layer model of Hsueh [42]. It shall be derived, to provide a reference for the coming models.

Hsueh's model predicts for κ the following equation:

$$\kappa = \frac{1}{r} = \frac{3[E_s(c-\alpha_s\Delta T)t_s^2 - \Sigma_{i=1}^n E_i t_i (c-\alpha_i\Delta T)(2h_{i-1}+t_i)]}{E_s t_s^2(2t_s+3h_b) + \Sigma_{i=1}^n E_i t_i[6h_{i-1}^2 + 6h_{i-1}t_i + 2t_i^2 - 3h_b(2h_{i-1}+t_i)]} \tag{2.6}$$

The Young's Modulus of the respective layer i is denoted by E_i, its coefficient of thermal expansion by α_i and its thickness by t_i. The difference in temperature is given by ΔT and h_i corresponds to a coordinate value in stacking direction of the film. The origin of this system would be the interface between substrate (subscript s) and the first layer, as can be seen in figure 2.1b.

The uniform strain component c can be calculated with equation

$$c = \frac{(E_s t_s \alpha_s + \Sigma_{i=1}^{n} E_i t_i \alpha_i)\Delta T}{E_s t_s + \Sigma_{i=1}^{n} E_i t_i} \tag{2.7}$$

and the location of the bending axis h_b can be derived from:

$$h_b = \frac{-E_s t_s^2 + \Sigma_{i=1}^{n} E_i t_i (2h_{i-1} + t_i)}{2(E_s t_s + \Sigma_{i=1}^{n} E_i t_i)} \tag{2.8}$$

Combining equations (2.6) to (2.8) gives a theoretical approximation of κ for a multilayer structure at a given temperature.

Hsueh also provides a set of equations to calculate the stresses within the individual layers:

$$\sigma_{s,i} = E_{s,i}(\epsilon - \alpha_{s,i}\Delta T) \tag{2.9}$$

with strain ϵ being

$$\epsilon = c + (h - h_b)\kappa. \tag{2.10}$$

Equation (2.9) holds for substrate and film respectively.

2.4.2. Elastic response

In the previous section the elastic model according to Hsueh was derived. It is suited for multilayer structures independent of layer count. Kirchgaßner also tried to approximate the elastic response using a bilayer model proposed by Chu [41]. As already mentioned, the model was not well suited for the task, as plastification in the copper layer sets in. Another reason to extend the bilayer model to three layers are the significant residual stresses caused by deposition of TiW in the TiW layer (σ_{TiW}). In the following paragraphs this model shall be derived. As a reference the stress-strain behaviour of the elastic and the plastic system is sketched in figure 2.3.

The stress fields in elastic response can be described by this set of equations. The numbering refers to the layer system, Si being 1, TiW 2 and Cu 3.

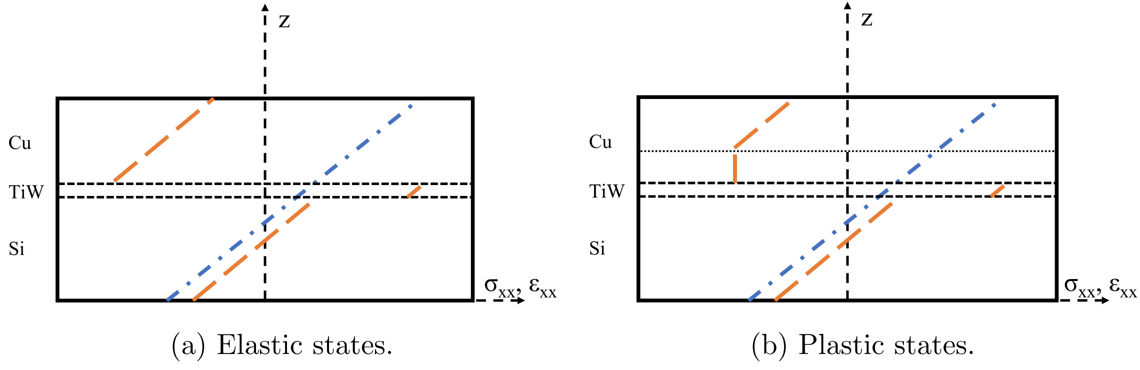

(a) Elastic states.

(b) Plastic states.

Figure 2.3.: Stress and strain trends in a bent beam. Blue (dash-dotted) shows the continuous strains in the beam, and orange (long dashes) depicts stresses. Short dashes in black show the single layers of the material architecture. In (b) the black dotted line shows the elastic-plastic transition.

$$\sigma_{xx,1}(z) = E_1 \left[\left(z - {}^{t_1}\!/\!_2\right) \kappa + \epsilon_1 \right] \tag{2.11a}$$

$$\sigma_{xx,2}(z) = E_2 \left[\left(z - \left(t_1 + {}^{t_2}\!/\!_2\right)\right) \kappa + \epsilon_2 \right] + \sigma_{TiW} \tag{2.11b}$$

$$\sigma_{xx,3}(z) = E_3 \left[\left(z - \left(t_1 + t_2 + {}^{t_3}\!/\!_2\right)\right) \kappa + \epsilon_3 \right] \tag{2.11c}$$

The model bases on the assumption that no delamination occurs and therefore strain is continuous at the interfaces.

$$\epsilon_{xx,1}(z = t_1) = \epsilon_{xx,2}(z = t_1) \tag{2.12a}$$

$$\epsilon_{xx,2}(z = t_1 + h_2) = \epsilon_{xx,3}(z = t_1 + t_2) \tag{2.12b}$$

with

$$\epsilon_{xx,1}(z) = \left(z - {}^{t_1}\!/\!_2\right) \kappa + \epsilon_1 + \alpha_1 \Delta T \tag{2.13a}$$

$$\epsilon_{xx,2}(z) = \left(z - \left(t_1 + {}^{t_2}\!/\!_2\right)\right) \kappa + \epsilon_2 + \alpha_2 \Delta T \tag{2.13b}$$

$$\epsilon_{xx,3}(z) = \left(z - \left(t_1 + t_2 + {}^{t_3}\!/\!_2\right)\right) \kappa + \epsilon_3 + \alpha_3 \Delta T \tag{2.13c}$$

As the beam is in a force equilibrium the following equation is zero.

$$\Sigma F = 0 = E_1 t_1 \epsilon_1 + E_2 t_2 \epsilon_2 + E_3 t_3 \epsilon_3 + \sigma_{TiW} t_2 \tag{2.14}$$

The curvature, the thicknesses and ΔT are measured, the respective Young's moduli and α of the layers are known reducing equations (2.11a) to (2.11c), (2.12a) and (2.12b)

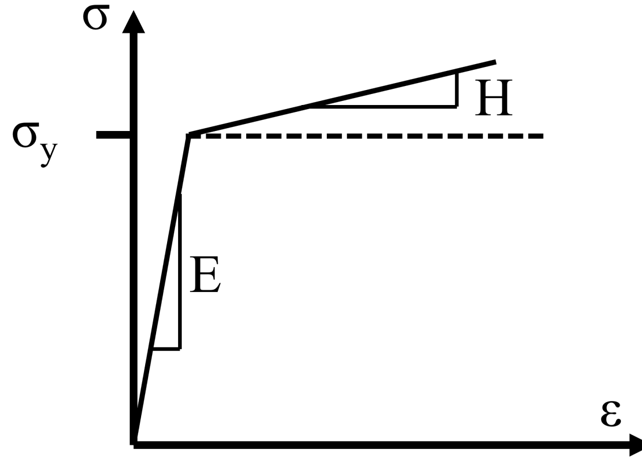

Figure 2.4.: Sketch of a bilinear stress-strain curve. H depicts the plastic modulus. The dashed line shows an idealized perfectly plastic response.

as well as (2.14) to a system of six variables. Thus, the system is solvable analytically.

2.4.3. Plastic response

It can be seen later (it is referred to figure 4.1), that the curvature deviates from a linear trend and flattens out. This can be attributed to the plastification of a layer, which is backed by findings in literature [14, 43]. Both Si and TiW have higher yield strengths than copper, so the model shall be extended to describe the plastification of the copper layer.

For simplicity a bilinear stress-strain model (figure 2.4) shall be used. After yielding, stress increases linearly with strain, but with another modulus. This simplification is closer to experimental findings compared to a perfectly elastic-plastic approximation as the ultimate tensile strength (UTS) of this material is nearly double its yield strength at room temperature, indicating significant hardening [33]. The modulus after yielding H_3 can be estimated by using available experimental data about yield strength σ_y, UTS and strain at these values which can be found in [33].

The copper layer will plastify first at the TiW-Cu interface as the compressional stresses are the largest there (compare figure 2.3b). This section will be treated as a fourth elastic layer due to the bilinear stress-strain model. Therefore, some equations from the previous section have to be adapted and new ones can be found.

Equation (2.11c) is split into:

$$\sigma_{xx,3} = \begin{cases} H_3\left[\left(z - \left(t_1 + t_2 + {}^{t_3}\!/_2\right)\right)\kappa + \epsilon_3\right] + \sigma_{y,3} + \sigma_h & (\sigma_{xx,3} > \sigma_{y,3} + \sigma_h) \quad (2.15a) \\ E_3\left[\left(z - \left(t_1 + t_2 + {}^{t_3}\!/_2\right)\right)\kappa + \epsilon_3\right] + \sigma_h & (\sigma_{xx,3} \leq \sigma_{y,3} + \sigma_h) \quad (2.15b) \end{cases}$$

σ_h being the residual stresses induced into the plastified Cu layer following previous heating cycles. Those stresses are calculated using a hysteresis in the stress strain curve (more detail in section 4.2).
Finally, more terms get added to equation (2.14):

$$\Sigma F = 0 = E_1 t_1 \epsilon_1 + E_2 t_2 \epsilon_2 + t_3 \epsilon_3 \left(x H_3 + (1-x) E_3\right) + \sigma_{TiW} t_2 + \sigma_{y,3} t_3 + \sigma_h t_3 \tag{2.16}$$

The normalized plastified share of the Cu layer is depicted by x.
Equations (2.11a), (2.11b), (2.15a) combined with (2.15b), (2.12a), (2.12b) and (2.16) are leaving us at six equations for seven variables. Therefore, this system is only solvable numerically. This is performed by solving for zero in equation (2.16) using the Newton method.
It should be highlighted that the residual stresses in the TiW layer are known from other experiments. Later it will be discussed why the proposed model in combination with the conducted experiments is not quite sufficient to derive them as well. But an alternative experimental setup is suggested for the future. In the appendices the necessary equation system for solving with unknown residual stresses is included.

3. Experimental methods

The next section will give an overview over the sample preparation and the experimental parameters and setup as well as information regarding semi-automated image processing and FEA simulation.

3.1. Sample preparation

The wafer architecture is described in chapter 2.3. Small samples (approximately 3 by 10 mm) were broken out of the wafer and put into a brass holder for further processing. This included laser ablation [44] performed on the Auriga laser platform (Zeiss, Oberkochen, Germany) for rough cutting. The final geometry as well as cuts which were used for EBSD measurements were produced by focused ion beam (FIB) milling (LEO 1540 XB, Carl Zeiss, Oberkochen, Germany). The current used ranges from 500 pA to 20 nA. The desired beam geometry was about 100 µm in length and the layers of Cu and Si having a thickness of 4 µm respectively, the aim for width was around 5 µm. To encourage crack initiation a notch was added to some samples. The notching was performed with a 500 pA current positioned in the copper layer close to the TiW interface. By moving the beam up and down a 500 nm high and 7 µm wide notch could be produced, sitting at the interface between copper and TiW. The sample width was therefore limited to 4 µm, due to tapering within the notch.
The position of the notch was chosen to be at approximately 75 % of the beam length which is around 65 to 75 µm depending on final beam length. This position emerges from a compromise between the maximum strains due to thermal expansion at the tip of the beam and the constrain of these strains due to surrounding material, which

Table 3.1.: Geometries of the prepared samples. VB stands for vacuum break.

Sample	Length in µm	Width in µm	t_{Si} in µm	t_{TiW} in µm	t_{Cu} in µm
CuTiW	97.14	9.00	3.86	0.25	3.96
CuTiW-Notch	96.94	3.17	4.61	0.26	4.79
CuTiW-VB	95.16	7.40	4.67	0.24	4.53
CuTiW-VB-Notch	99.31	3.63	4.84	0.25	5.44

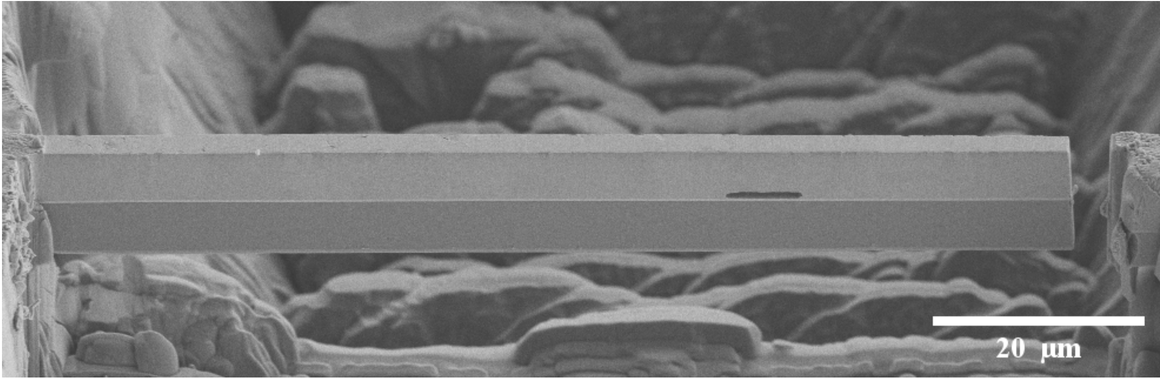

Figure 3.1.: Example of a sample with notch, slightly tilted at 1000x magnification. The bottom of the beam is the Si layer, followed by TiW and Cu.

would be maximized in the middle of the beam.

An example for a resulting beam can be seen in figure 3.1. The geometry of the four beams is listed in table 3.1.

3.2. Heating and EBSD measurement

The processed samples were tested in a heating apparatus which allows for in-situ SEM imaging. This sample holder is described in great detail in [45], but nevertheless a brief overview shall be given. The holder is made of V and the sample is fixed with a ceramic screw. Below the screw, a Type K (Chromel/Alumel) thermocouple is brazed on the holder. A few coils of Konstatan®around the holder are used for inductive heating. The power supply is connected via thicker copper wires, which can be fed through the SEM (Zeiss LEO 982, Oberkochen, Germany) chamber door. This is also true for the thermocouple wires.

Outside the SEM the thermocouple connects to an USB TC-08 data logger (Pico Technology, St. Neots, UK) which allows for a connection via USB to a laptop. The power is given by a TOE 8952-20 dual output DC power supply (Toellner Electronic Instruments GmbH, Herdecke, Germany) which is able to provide 0 to 20 V in a current range of 0 to 20 A. The monitoring of the temperature as well as the regulation of the power output is enabled by a LabView®program (National Instruments Corp., Austin, Texas, USA) running on mentioned laptop.

When mounted, the samples were allowed to acclimatize in the SEM for at least 48 h. The reason for this long time span is the high temperature to which the sample will be heated during the experiments. One cycle of heating consists of a step wise increase in temperature from room temperature at around 22-24 °C to 400 °C. At 400 °C organic residues on the sample as well as on the holder and thermocouple system including

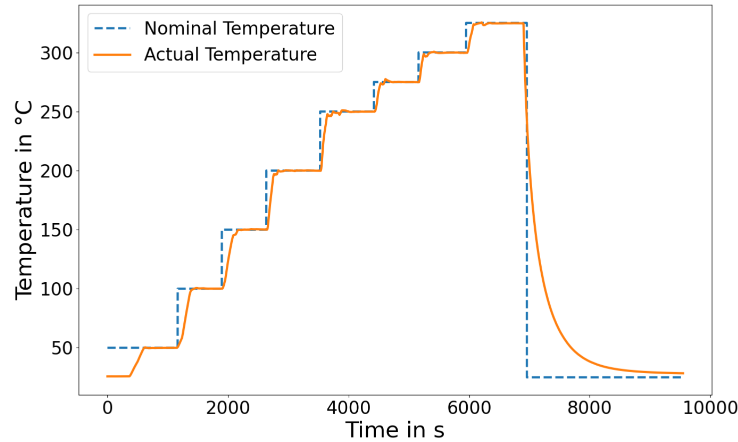

Figure 3.2.: Exemplary Heating Cycle.

the connecting wires, can evaporate and increase the pressure in the vacuum chamber. When it gets above a critical value, a kind of emergency venting can happen and the electron beam is turned off. The longer the setup is in the chamber prior to testing, the more stable is the vacuum at higher temperatures. This circumstance and the lack of acclimatization time leads to the early abortion of some cycles.

In figure 3.2 an exemplary heating cycle can be seen. Starting from room temperature, SEM images of the sample were taken. An initial heating to 50 °C was followed by 50 °C steps to 250 °C. At this point, the pressure in the vacuum chamber was slowly increasing, which led to a more cautious approach with 25 °C steps up to 400 °C. When this temperature was reached in an earlier cycle, the reduction in step size was ignored and 50 °C steps were used up to the final temperature. Between steps the sample was allowed to fully settle at a given temperature for a couple of minutes, before high resolution images were taken.

In total three cycles were performed per sample. Between the cycles the sample was passively cooled via thermal radiation and conduction through the holder.

To observe microstructural changes in the copper layer, EBSD scans (SEM: Tescan Magna, Tescan Orsay Holding, Brno, Czech Republic, EBSD: Bruker Quantax, Bruker Corporation, Billerica, USA) were performed before and after testing. Sections around the notches as well as areas prepared for EBSD examination were scanned. The images were taken at a tilt angle of 65° as the sample including the holder was not able to be tilted to the usually used 70°. The overview images for general microstructural characterization were taken with a resolution of 100 nm and the area around the notches with 50 nm. The results were reasonably good at a combination of 20 mm EBSD detector distance and 20 mm electron beam working distance.

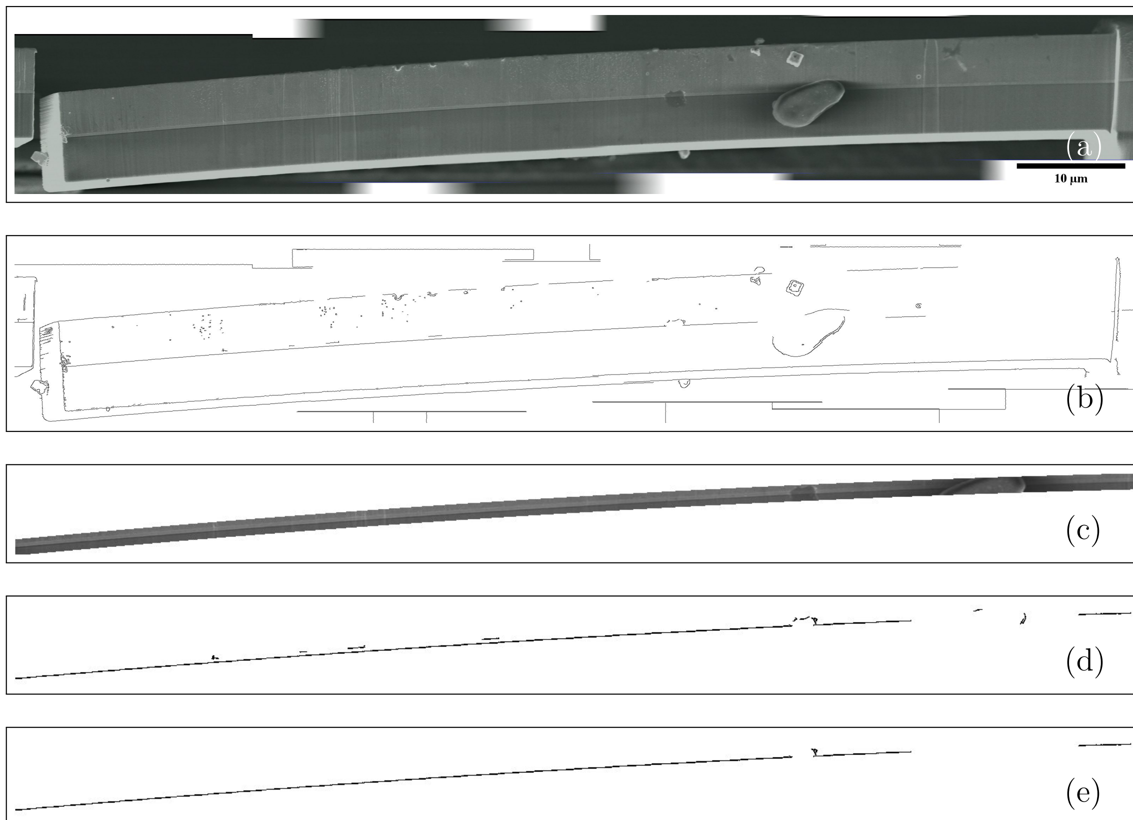

Figure 3.3.: The working process of the semi-automated curvature detection program. In (a) the original image can be seen. The process consists of a Canny edge detection step (b), followed by masking (c) and conversion to binary (d). Finally a connecting composites algorithm leaves only edges belonging to the interface. The scale bar in (a) is representative for all figures.

3.3. Image processing

The in-situ SEM images were used to derive the curvature of the beam. This task was performed by Kirchgaßner manually by setting points on an image of low magnification (1000x). The process was improved upon by a three-stage plan: In the first stage images which display a part of the beam at high magnification and resolution are stitched manually together via paint.net. Linear blending was applied to smooth the transitions at the overlaps. In the second stage a semi-automatic Python program (Python 3.8) with graphical user interface was programmed. The goal is to detect the SiO_x-TiW interface as it shows the highest amount of contrast. Several steps are used to get the location of this interface.

Canny Edge Detection Algorithm The used Canny Edge Detection Algorithm is based on [46]. It is incorporated in the opencv package (version 4.0.1) available in Python 3.8. The processing steps include noise reduction (Gaussian 5x5 filter) and the evaluation of intensity gradient in x- and y-direction with a Sobel

filter. This reveals the magnitude and direction of intensity changes. In a next step possible edges are compared to its neighboring pixels in gradient direction. As a result, the edges get very thin. After this point, the algorithm needs a user input: a minimum value and a maximum value for edge detection. Edges with intensity changes above the maximum value are considered as 'true' edges while intensity changes above the minimum value are only considered as 'true' edges if they are connected to an edge with an intensity change above maximum value. A manual insertion of these values is necessary as the contrast and brightness settings not only differ from stitched image to image but also within the image in the stitched sections, respectively. A representative result is shown in figure 3.3a.

Manual masking In the next step the user clicks at least three times at the portion of the image where the SiO_x-TiW interface is. This reduces the amount of computing power and time. The user is also able to disregard areas of low contrast or pollution on the sample. The image is inverted as this enhances the contrast on a computer monitor and makes for easier detection of the interface. After entering the coordinates via clicking, the program fits a parabola (least squares fit, numpy package, version 1.20.3) and creates an inverted mask of this parabola $\pm$ 10 pixels (compare figure 3.3c).

Binary Conversion The mask is applied to the image generated by the Canny algorithm, which is a greyscale output as the binary image is stretched to the monitor size it is viewed on. The user inputs a value between 0 and 255 to turn pixels above the entered value into 255 valued pixels (as seen in figure 3.3d). The higher the value, less pixels will be considered as edges and they will be thinner. This is necessary to be done manually as it is closely tied to the next step.

Connecting composites algorithm The user can then enter a value between 0 and 1, which is related to the largest connecting pixel agglomeration (value of 255) in the binary image. Several functions from the ndimage class included in the scipy package (version 1.7.1) are used to detect and reset smaller islands to value 0. This step is used to remove artefacts or pollution edges if possible. An exact coordination of the previous steps is necessary, most importantly the conversion to binary in the step prior is very important, as this can generate thick connecting parts of the interface or small, thin and separated parts, which will be easily deleted in this step if not careful. The result is a binary image of the SiO_x-TiW interface, which can be used to fit the parabolic curvature (figure 3.3e).

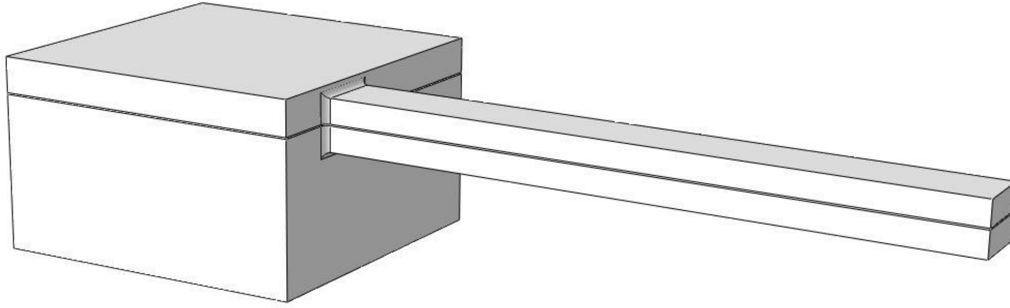

Figure 3.4.: Exemplary image of a FEA model. From bottom to top one can see the Si wafer, the TiW diffusion layer and the Cu metallization.

3.4. Finite element analysis

To further underline the experimental results a FEA was performed using ABAQUS (Dassault Systèmes SE, France). Several models were evaluated, starting with a simple 2D model of a beam, which is rigidly fixed on one side. The same boundary condition was applied in a 3D model. To get closer to the experimental setup, it was decided to model a part of the remaining wafer similar to simulations found in literature [47]. This means in detail, that a 50x50x50 µm part of the wafer is simulated as well, as can be seen in figure 3.4.

All models are inspired by the experiments, so the geometric measurements of the beams can be taken from table 3.1 and the applied temperature loads correspond to table 4.1. The beam is not positioned in the middle of the bulk wafer part, as this is not the case in the experiments. As offset from the front edge of the wafer 10 µm are approximated. The radius between wafer and beam was estimated to be around 1-1.5 µm, depending on the model. The notch was also rounded to a radius of 0.2 µm.

Regarding the material properties, linear elastic behaviour was assumed for the Si and the TiW layer. The Cu layer experiences plastic deformation during heating and this was estimated as perfectly elastic-plastic (compare figure 2.4). Additionally, the point of plastic yield is temperature dependent. This temperature dependent data can be found in [30]. Used parameters are listed in table 3.2 for convenience.

Attention was paid to the element size especially in the thin TiW layer and around the notches. It was ensured that at least five elements were used per layer and the notches were meshed with a finer element size. The elements used were hexagonal linear ones as this led to sufficient results.

The internal compressive stresses in the TiW layer were modelled by assuming a biaxial stress state of the magnitude $-1.5\,\text{GPa}$ [23].

Table 3.2.: Mechanical properties of the layers.

Material	E in GPa	ν -	α in $^{W}/_{\mathrm{mK}} \cdot 10^{-6}$	T in °C	σ_y in MPa
Si	170	0.25	2.6	-	-
TiW	330	0.34	4.5	-	-
Cu	110	0.35	16.7	20 100 125 150 200 400	142 140 130 125 107 79

The boundary conditions of the 3D-models with bulk wafer were chosen to restrict translational movement on three sides (all not visible in figure 3.4) in the direction normal to that plane. This comes closest to a homogeneously expanding volume of material behind these planes. It should be mentioned however, that these conditions are generating a stiffer model as in reality, as the surrounding material is also heated and can deform elastically. Nonetheless it is the opinion of the author that this model represents the experiment sufficiently well without oversimplification.

4. Results

The next section lists the gathered results from the cyclic heating experiments, it highlights similarities and differences between the proposed analytical and the numerical FEA model as well as give examples for microstructural indication of thermo-mechanical fatigue.

4.1. Beam curvature

While repeatedly heating the samples, in-situ images were gathered and processed as described earlier. The maximum temperatures reached per cycle are listed in table 4.1. The resulting curvature values can be seen in figure 4.1. In addition to experimental results (triangles), an elastic approximation by Hsueh (black line) and the FEA results (trigonal symbols) are added. Each cycle is depicted with a different symbol and color, which is also true for the experimentally gathered data.
Hsuehs' model is an elastic approximation and therefore independent of the cycle number. It is however different for each sample as their individual geometry is playing a significant role. The used sample dimensions can be found in table 3.1.
The FEA model is in very close resemblance to the elastic approximation. At low temperatures it shows a slightly larger slope, but with increasing temperature it approaches Hsuehs' model. After unloading a small negative curvature is calculated, which resembles an upwards bending beam independent of the sample. Accordingly, the third cycle is shifted to smaller curvature values.
The experimental data shows initial curvature values deviating from zero, which is in contrast to the proposed elastic and numeric models. CuTiW shows an initial

Table 4.1.: Maximum temperatures reached in each cycle.

Sample	T_{max} Cycle 1 in °C	T_{max} Cycle 2 in °C	T_{max} Cycle 3 in °C
CuTiW	275	400	400
CuTiW-Notch	325	350	350
CuTiW-VB	400	400	400
CuTiW-VB-Notch	325	350	370

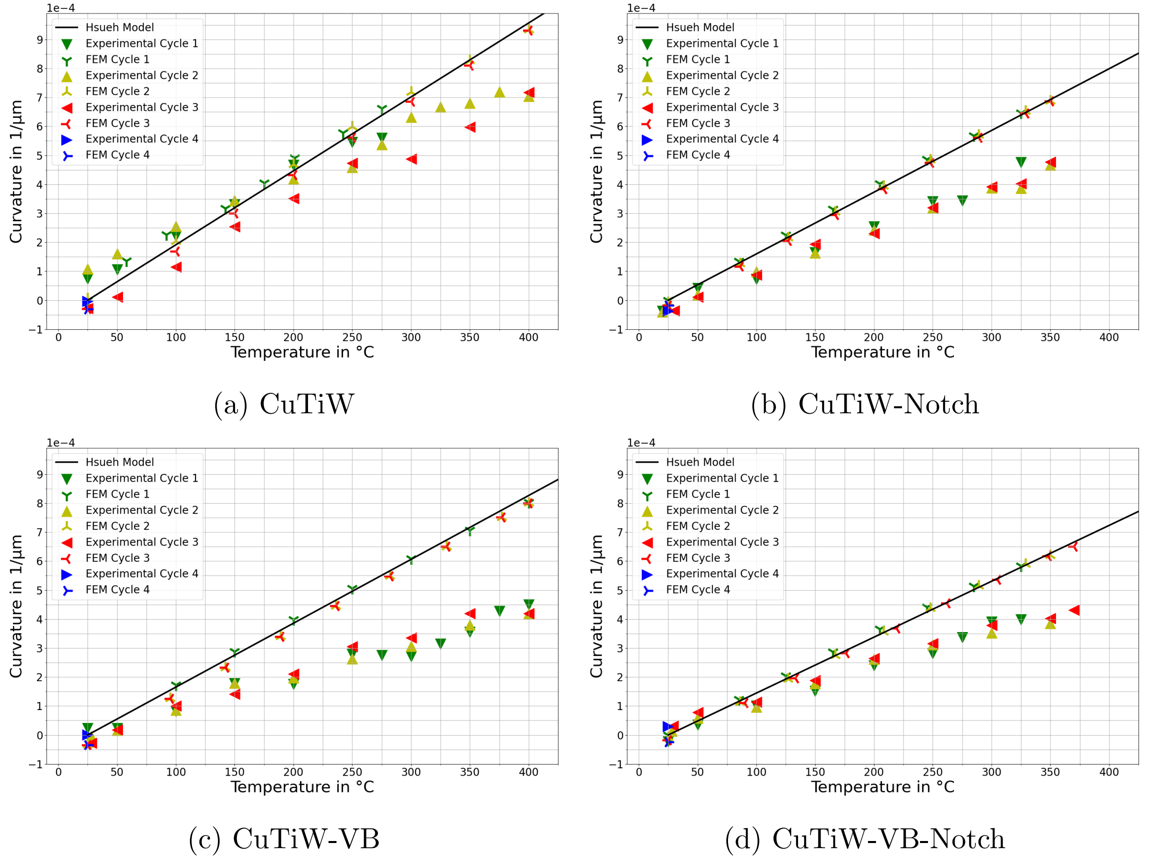

(a) CuTiW (b) CuTiW-Notch

(c) CuTiW-VB (d) CuTiW-VB-Notch

Figure 4.1.: Curvature values from experiment and FEA in $^{10^{-4}}/_{\mu m}$. For comparison the elastic model of Hsueh is shown as a black line.

downwards curvature of $\kappa \approx 1 \times 10^{-4}\,{}^{1}/_{\mu m}$, which decreases to essentially $\kappa \approx 0\,{}^{1}/_{\mu m}$ in cycle three and four. In the case of the other samples the curvature at room temperature is smaller, with $\kappa = \pm 0.3 \times 10^{-4}\,{}^{1}/_{\mu m}$ in the beginning and remaining in this regime until the end of the experiment. For these samples, the difference between cycles is in the same order of magnitude as for the FEA simulations, but the FEA model shows larger curvature values especially at high temperatures. The maximum reached curvature values depend on maximum temperature as well as sample geometry and the general trend is comparable to the elastic model and the FEA simulation. In the experimental data error bars are dismissed, as the symbols are approximately as large as the largest errors.

After an initial linear increase in curvature all samples show a reduced increase in curvature with rising temperature and experiment and elastic model deviate significantly from each other. The onset temperature of this behaviour differs from sample to sample, as well as between cycles. In general, it can be stated that later cycles need higher temperatures for the deviation from the initial linear increase in curvature, as can be seen in figure 4.1. At elevated temperatures, the curvature reaches a plateau, which again is pushed to higher temperatures for later cycles. In the case of CuTiW and

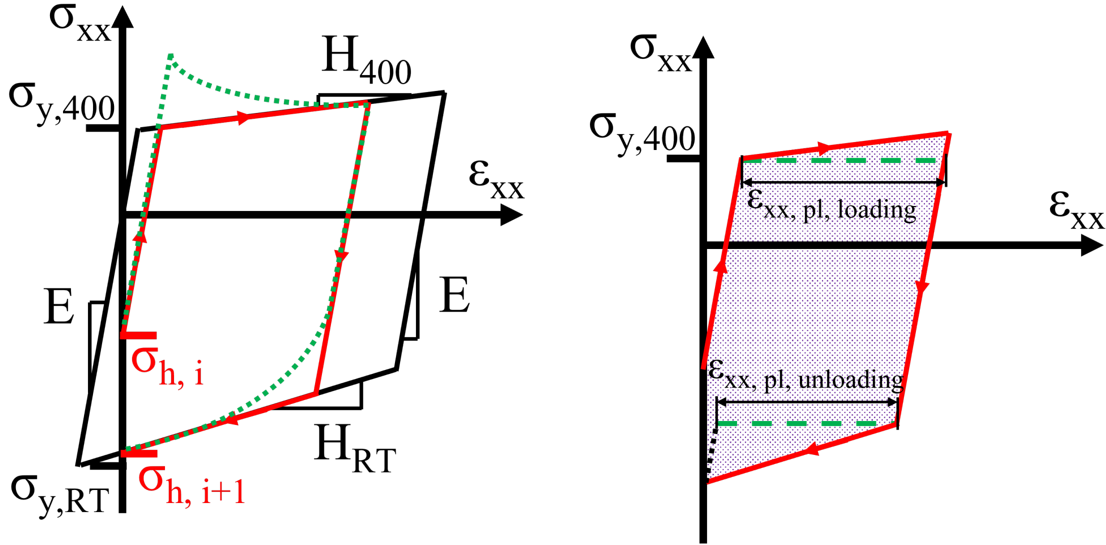

(a) The hysteresis curve during a heating cycle. Considering this behaviour, residual plastic stresses σ_h can be calculated. The dotted green line shows the actual behaviour, while the red line shows the approximated model, which is sufficient for calculations.

(b) Dissipated energy (shaded area) and plastic strain (dashed green lines) added to the material during a heating cycle.

Figure 4.2.

CuTiW-Notch (figures 4.1a and 4.1b) this plateau is not reached in the third cycle.

4.2. Internal stress distributions

This section presents the results obtained using the model derived in chapter 2.4.3. Furthermore, the FEA model described in 3.4 is used for comparison.

Earlier the residual stresses in the copper layer σ_h due to plastic deformation have been introduced. In the following it is shortly explained how these are obtained for the analytical model. In section 2.4.3 it is established that Cu can be assumed to have a bilinear elastic-plastic response. In figure 4.2a this behaviour is extended to the case of unloading after heating the sample. The schematic shows the case for a heating to 400 °C.

We start the hysteresis with an arbitrary value for σ_h, indicated by $\sigma_{h,i}$. Before the first curvature measurement this value is $\sigma_{h,i} = 0\,\text{MPa}$. Heating causes the material stack to curve, which increases the present stress. Simultaneously the yield strength decreases, and at some temperature T_i $\sigma_T = \sigma_{y,T}$ and plastic yield sets in. Increasing the temperature further lowers the yield strength and the material hardens as it is strained. This behaviour is depicted in figure 4.2a as a dotted green line, but it is not

relevant to the outcome of the calculation which is approximated by the red line.

At 400 °C a certain maximum stress is reached, which can be calculated considering the present residual stress $\sigma_{h,i}$, the yield strength at elevated temperature $\sigma_{y,400}$ and the bilinear moduli E and H_{400}. At this point it is important to remember that by definition of this model the elastic modulus is not temperature dependent in contrast to the plastic modulus, as it depends on fracture strain, yield strength and ultimate tensile strength.

When cooling the sample, we unload elastically. Either we reach $\epsilon_{xx} = 0$ without crossing the yield line, now defined by bilinear behaviour at room temperature (abbreviation RT in figure 4.2a), and the corresponding stress would be $\sigma_{h,i+1}$ for the next heating cycle. When crossing the yield limit, a similar consideration to the previous paragraph yields a maximum allowable residual stress. This yield limit is defined by the current temperature and its corresponding yield strength. Further cooling increases the yield strength and changes the corresponding plastic modulus (dotted green line in figure 4.2a). In the end the maximum allowable residual stress is defined by room temperature yield strength and plastic modulus, which is used for calculations (red line in figure 4.2a).

Cooling and unloading are implemented in two steps, as the strain at room temperature might not be zero due to some remaining curvature. First, the residual stresses for the next heating step are calculated as if $\kappa = 0$ and second, an elastic calculation is performed to adjust the residual stresses to the corresponding values.

Using the hysteresis area one can also calculate the dissipated energy (figure 4.2b shaded area) as well as the plastic strain (dashed green lines) per cycle.

Solving both the analytical model and the FEA model yields the results in figure 4.3. The data from the FEA model is taken from the middle of the beam inside the beam. The vertical axis shows the material architecture in µm starting with the substrate Si and the layers TiW and Cu. The horizontal axis depicts the stresses in beam direction herein referred to as σ_{xx}. The sample represented in figure 4.3 is CuTiW-Notch, but the trends are similar in the other samples as well. These can be found in chapter 5.3.3 and appendix B.

Both models agree with each other quite well. The Si layer carries very little stress, while the TiW film still possesses its high initial residual stress of around −1.5 GPa [23]. The FEA model reduces this stress by about 100 MPa. The snake like behaviour of the stress in the Cu layer is also captured by both models. It comprises of an elastic layer (I) with very little residual stresses, a layer with increasing plastification (II) and a region close to the Cu-TiW interface which is fully plastified and reaches the maximum value for σ_h (III). The models differ slightly concerning the thicknesses of

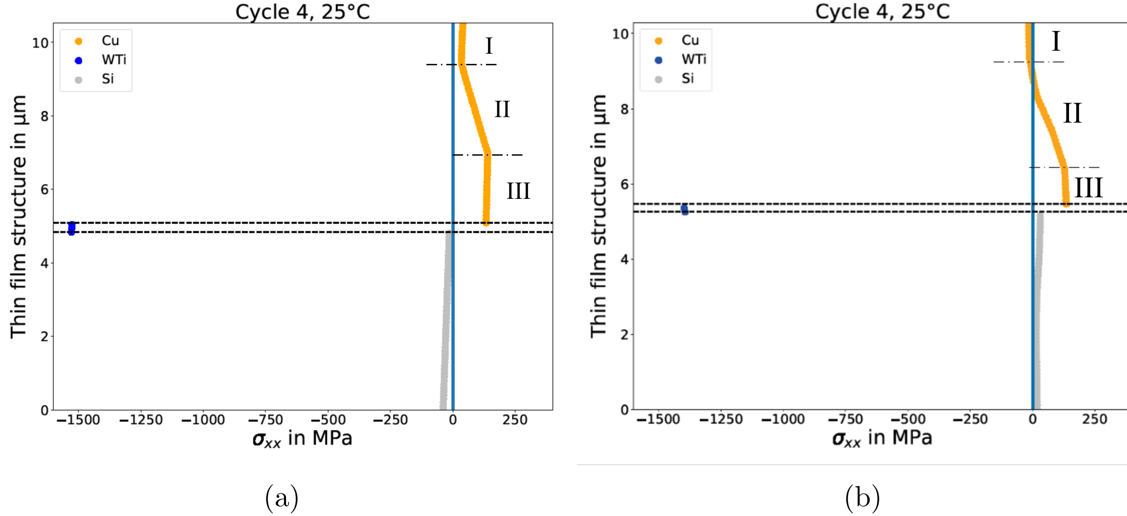

(a) (b)

Figure 4.3.: Stress distribution using the analytical model at room temperature after three cycles using experimental data from CuTiW-VB-Notch (a) and the FEA model for CuTiW-VB-Notch (b). Negative stresses depict compressive stresses. The interfaces are depicted by dashed black lines. The dash dotted lines divide the elastic (I) region, the region plastically deformed below maximum residual stress (II) and the region deformed to maximum residual stress (III).

these layers inside the Cu but both show $\sigma_{h,max}$ of around 140 MPa. It is referred to chapter 5.3.3 for more detailed investigations on the plastic behaviour of the Cu layer, the mechanisms causing it and the differences between the two models.

Using the herein acquired stress mismatch between TiW and Cu layer $\Delta\sigma_{xx}$, one can estimate the stress intensity factor K at the notches, using linear elastic fracture mechanics. It should be emphasized that this is an approximation, as some simplifications have to be made. It can be seen in figure 4.4 that a mode II configuration of a center cracked sample is the most appropriate model for the present case. First, linear elastic fracture appears only in brittle materials like ceramics and glasses, Cu on the other hand is quite ductile. Second, a uniaxial approach is chosen, which admittedly matches the approach for the analytical model providing $\Delta\sigma_{xx}$, but neglects any effects due to mode mixture. Third, the notch is positioned at the interface. This usually requires complicated bimaterial approaches, including Dundurs parameters [14]. It is however out of the scope of this work to dive deeper into this and for simple comparisons in section 5.3.4, these assumptions should suffice. The following equations are taken from [48]. K_{II} is calculated using

$$K_{II} = \tau\sqrt{\pi a}F\left({}^{a}/_{b}\right) \tag{4.1}$$

with the shear stress τ being

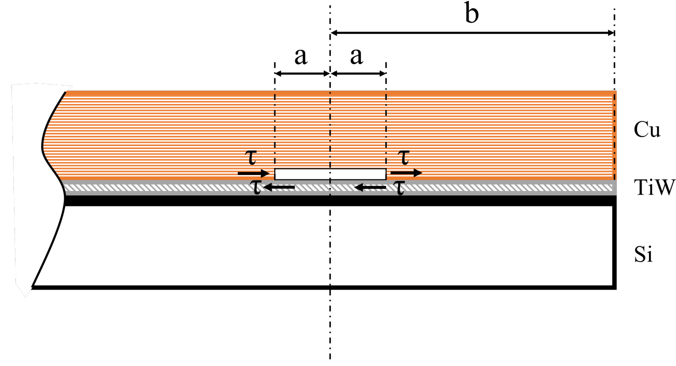

Figure 4.4.: The tip of a notched sample. From bottom to top Si (white), TiW (shaded grey) and Cu (shaded orange) is shown.

Table 4.2.: K_{II} values during experiment. RT stands for room temperature and HT for high temperature

Cycle and temperature	CuTiW-Notch in $\mathrm{MPa}\sqrt{\mathrm{m}}$	CuTiW-VB-Notch in $\mathrm{MPa}\sqrt{\mathrm{m}}$
1, RT	2.41	2.39
1, HT	1.58	1.62
2, RT	2.70	2.69
2, HT	1.59	1.64
3, RT	2.71	2.72
3, HT	1.56	1.62
4, RT	2.71	2.74

$$\tau = \frac{\Delta\sigma_{xx}}{2} \tag{4.2}$$

according to the maximum shear stress hypothesis after Tresca [49]. The geometrical parameters a and b can be seen in figure 4.4, a being half the length of the notch and b being the distance from notch centre to beam tip. $F\left({}^{a}/_{b}\right)$ is a correction factor depending on notch geometry. It can be derived with a 0.1 % accuracy for any ${}^{a}/_{b}$ [48] with:

$$F\left({}^{a}/_{b}\right) = \left\{1 - 0.025\left({}^{a}/_{b}\right)^2 + 0.06\left({}^{a}/_{b}\right)^4\right\}\sqrt{\sec\frac{\pi a}{2b}} \tag{4.3}$$

Using $\Delta\sigma_{xx}$ from the analytical model, equations (4.1) to (4.3) yield the results in table 4.2.

The values lie between 1.56 $\mathrm{MPa}\sqrt{\mathrm{m}}$ at high temperatures and 2.74 $\mathrm{MPa}\sqrt{\mathrm{m}}$ at room temperature. As the geometry of the specimen is independent of temperature, the stress intensity factor is directly proportional to τ, which is larger at low temperatures. After one cycle, K_{II} increases about 0.3 $\mathrm{MPa}\sqrt{\mathrm{m}}$ to a quite stable value of $K_{II} \approx 2.7\,\mathrm{MPa}\sqrt{\mathrm{m}}$ at room temperature. The high temperature value is always

$K_{II} \approx 1.6\,\mathrm{MPa}\sqrt{\mathrm{m}}$ and does not change with further cycling. Therefore, considering further cycling a fatigue stress intensity range of $\Delta K = 2.7\,\mathrm{MPa}\sqrt{\mathrm{m}} - 1.6\,\mathrm{MPa}\sqrt{\mathrm{m}} = 1.1\,\mathrm{MPa}\sqrt{\mathrm{m}}$ would be probed.

4.3. Microstructural changes

This section will highlight changes in the microstructure during heating to 400 °C using EBSD scans and in-situ as well as postmortem SEM images. An overview of all samples after deformation is given in figure 4.5. In the images examples of voids at grain boundaries and the Cu-TiW interface and extrusions in Cu and Si layer can be observed. Additionally, a stable grain structure and the formation of nanopores in the Cu surface is observed. In the following paragraphs more detailed images of the ongoing processes are presented.

In section 3.2 it is explained that due to shading of the undercutted sample geometry the tilt angle during the EBSD measurements was only 65° instead of usually used 70°. This circumstance and the thin geometry of the Cu layer contributed to a decrease in image quality. Therefore, images of some samples turned out not useful for evaluation. Nevertheless, the band contrast maps of the other samples are shown in 4.6. 4.6a shows the grain structure before the heating cycles and figure 4.6b afterwards. It should be noted that a steady drift of the electron beam distorted the data in the vertical direction. Thus, a quantitative statement is not possible and scale bars are also excluded. The range of the horizontal image edge is around 10 to 15 µm and the portrayed height is between 4 and 5 µm. The images were assessed with Atex software version 3.25 [50]. A noise reduction including zero solution correction was performed. To emphasize the boundaries the images were smoothed and the contrast enhanced.

Despite the drawbacks during image acquisition a qualitative remark can be made to the extent that no grain growth is happening. Comparing the respective images in 4.6a and 4.6b one can see the same structures in the Cu layer. The visible distortion stems from the mentioned reasons.

EBSD is also able to detect differences in crystal orientation. Figure 4.7 shows the inverse pole figure maps around the notch area of sample CuTiW-VB-Notch. Again, a very stable microstructure in the Cu film can be observed. There are no changes in orientation in the respective grains. Smaller grains above the notch seem to disappear during heating, but this could be attributed to the lower resolution in figure 4.7a.

During heating void formation at boundaries can be observed. In figure 4.8 examples for this behaviour are shown. 4.8a shows the opposing stump of the CuTiW-VB beam. Gaps can be seen at grain boundaries and the interface (arrows). In figure 4.8b the

top of the beginning of the beam (CuTiW-VB) is displayed. Here pore-like voids are found especially at grain boundaries. The same is true for sample CuTiW-VB-Notch in figure 4.8c where gaps form explicitly at grain boundaries. The samples, which did not experience the vacuum brake during deposition display this behaviour only to a restricted extent. For exemplary reasons only larger voids are shown. One can also see cleavage between redeposited material and original Cu layer in figures 4.8a and 4.8c (dashed rectangles).

Using in-situ imaging it is possible to determine the starting temperature for void formation. For CuTiW-Notch this was 275 °C (in the first cycle) with growth to the maximum measured temperature of 350 °C (location on the opposing stump), while CuTiW shows no opening grain boundaries in the in-situ field of view. The beams of CuTiW-VB/-Notch also show no voids between grains, but the opening

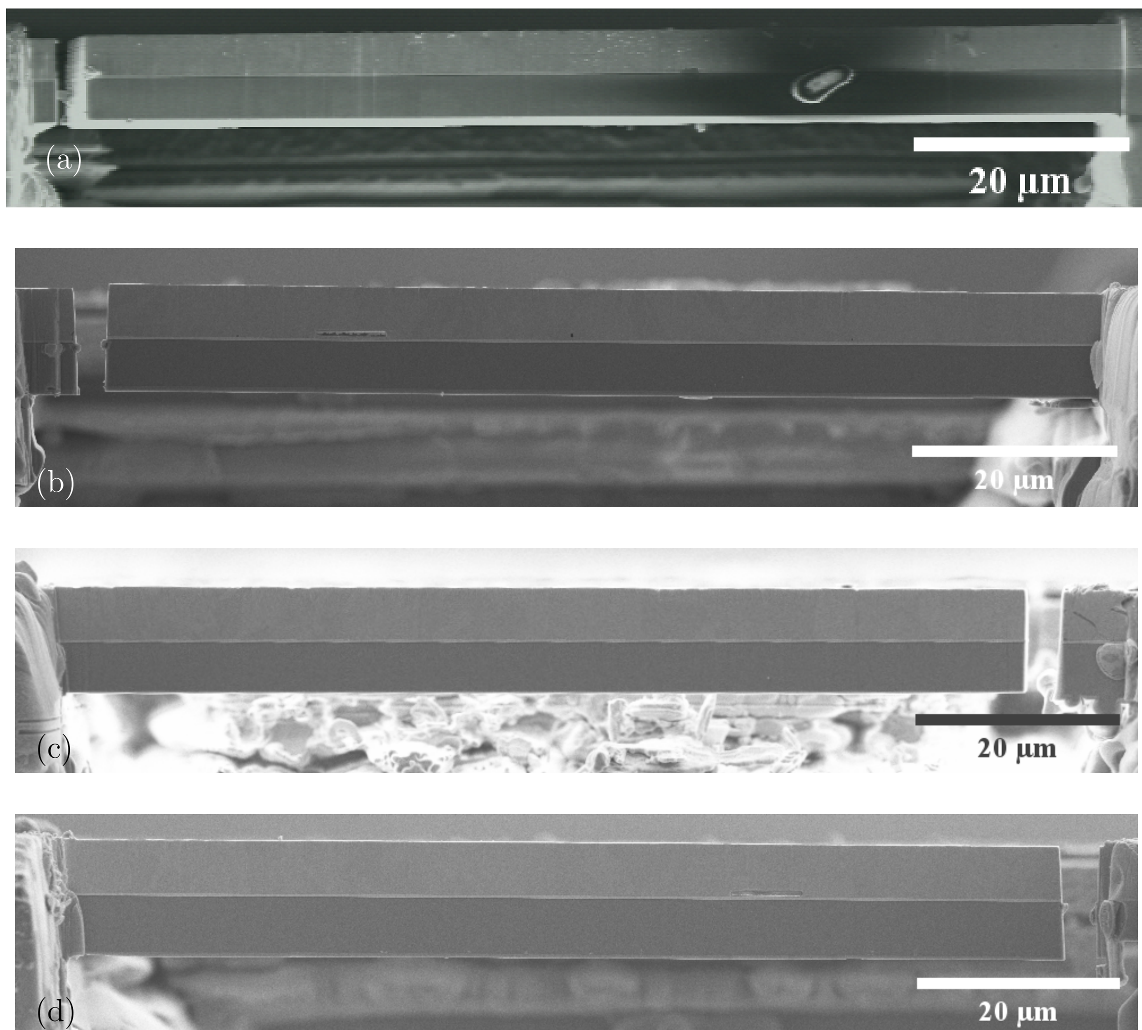

Figure 4.5.: SEM overviews of the post experiment samples at 1000x magnification. Samples CuTiW (a), CuTiW-Notch (b), CuTiW-VB (c) and CuTiW-VB-Notch (d).

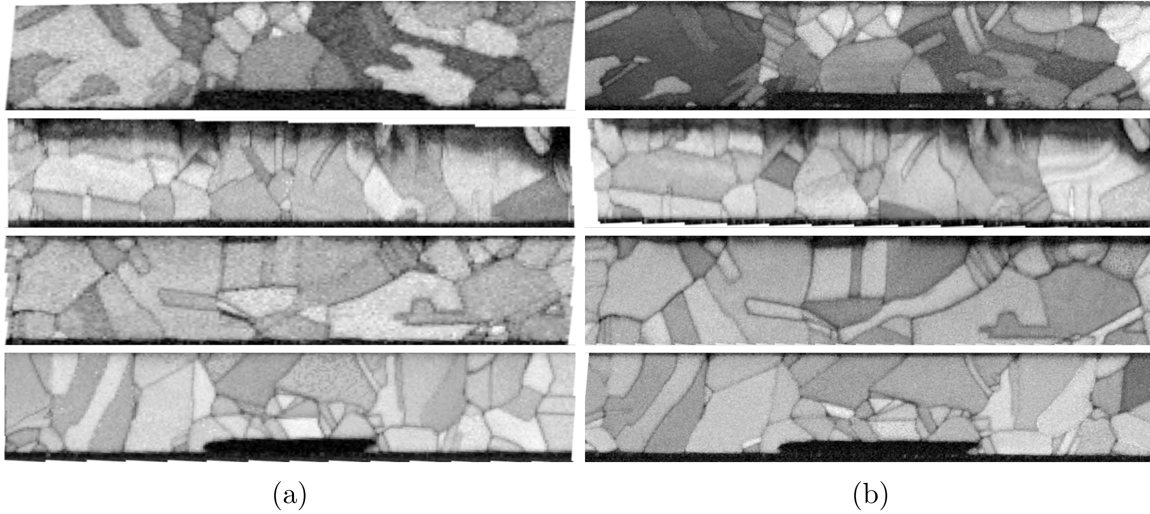

(a) (b)

Figure 4.6.: Band Contrast Maps acquired by EBSD before (a) and after (b) the experiment. From top to bottom it is CuTiW-Notch around the notch area, CuTiW-VB, CuTiW-VB-Notch, CuTiW-VB-Notch around the notch area. The image width is in the magnitude of 10-15 µm.

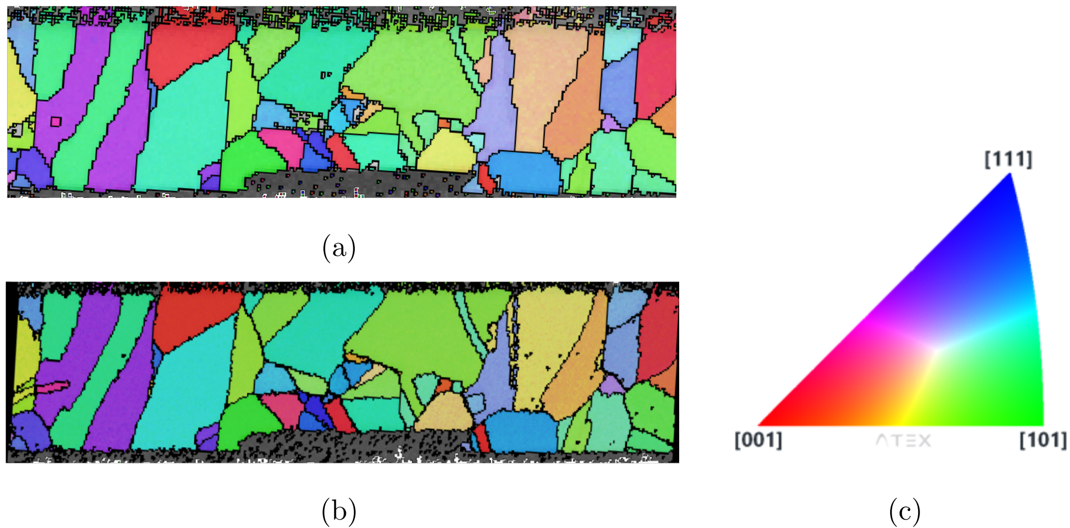

(a) (b) (c)

Figure 4.7.: Before (a) and after (b) heating inverse pole figure maps from sample CuTiW-VB-Notch around the notch area. (c) shows the inverse pole legend.

grain boundaries on the stump (figure 4.8a) open at 375 °C in the first cycle. As the maximum temperatures in the next cycles are not higher than the first one, no growth in the following cycles of this gap occurred.

A similar phenomenon can be observed in postmortem top view images shown in 4.9: (a) and (b) display sections of the beam and opposing stump of CuTiW-Notch, (c) and (d) are unprepared Cu surface and a beam section of CuTiW-VB. The grain boundaries are visible due to rounding. Some grains are even elevated and others are sunken in. It is not possible to define a set on temperature for this behaviour as the

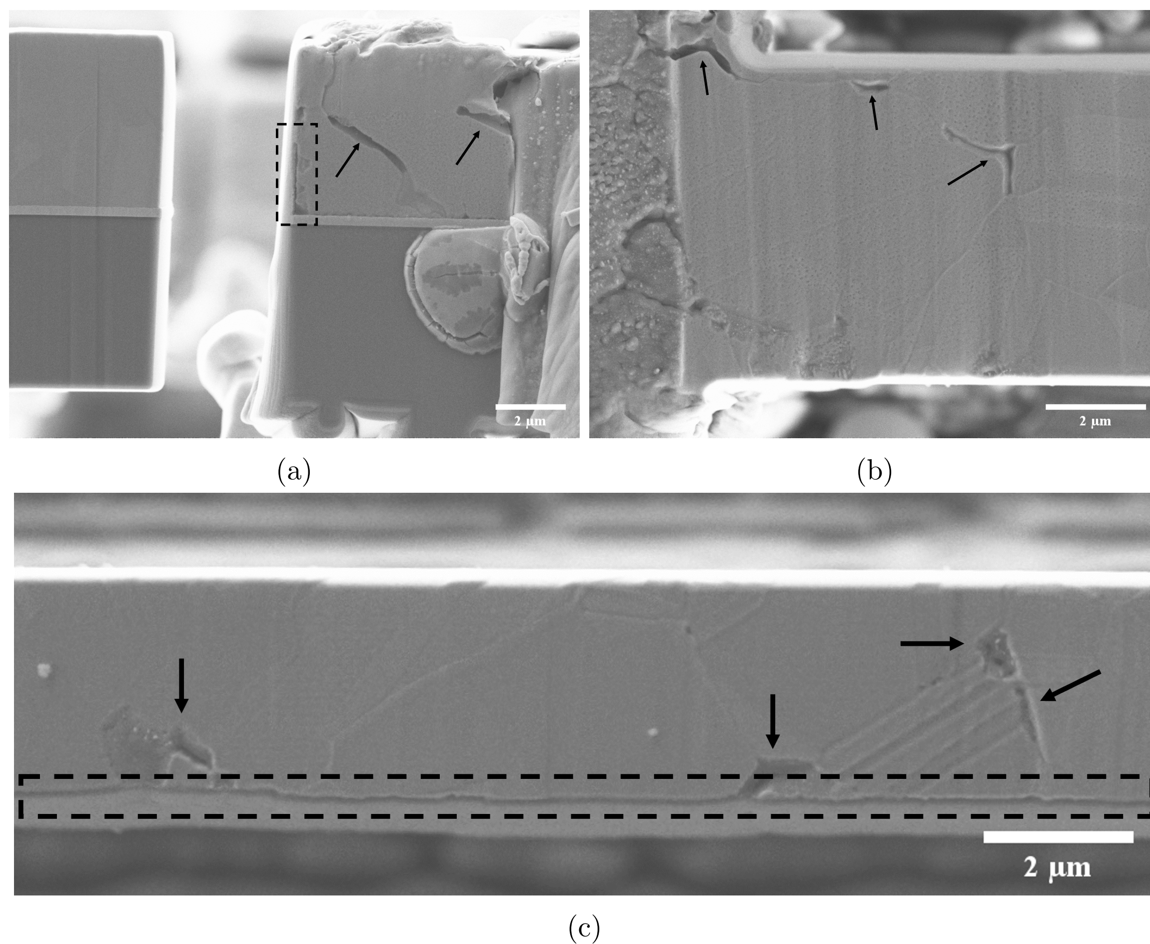

(a) (b)

(c)

Figure 4.8.: Examples for void formation. (a) (front view) and (b) (top view) are sections from CuTiW-VB at 7000x and 10000x magnification respectively and (c) is a top view of sample CuTiW-VB-Notch at 7000x magnification. Arrows point at voids at grain boundaries and the rectangular dashed regions show cleavage between redeposited material and original Cu layer.

top view is restricted to postmortem images only. In figures 4.9b and 4.9d additional example voids at grain boundaries can be found (arrows).

On the top of sample CuTiW-VB the formation of small pores can be observed (compare figure 4.9d). Those pores are not present on any other sample. As it is again the top side of the Cu layer it is not possible to determine the cycle or temperature this feature appears first.

Two samples have been notched to encourage crack initiation at the interface resulting in delamination. This could not be observed, however material flow was detected. Figure 4.10 shows both notches in detail. During heating cycles material wanders from below into the empty notch space. The amount of material is greater in sample CuTiW-Notch. In those images it is also evident, that the placement of the notch is not very trivial and in case of the CuTiW-Notch sample it has been placed a couple of hundred nanometers inside the Cu layer. The first appearance of the extrusions in

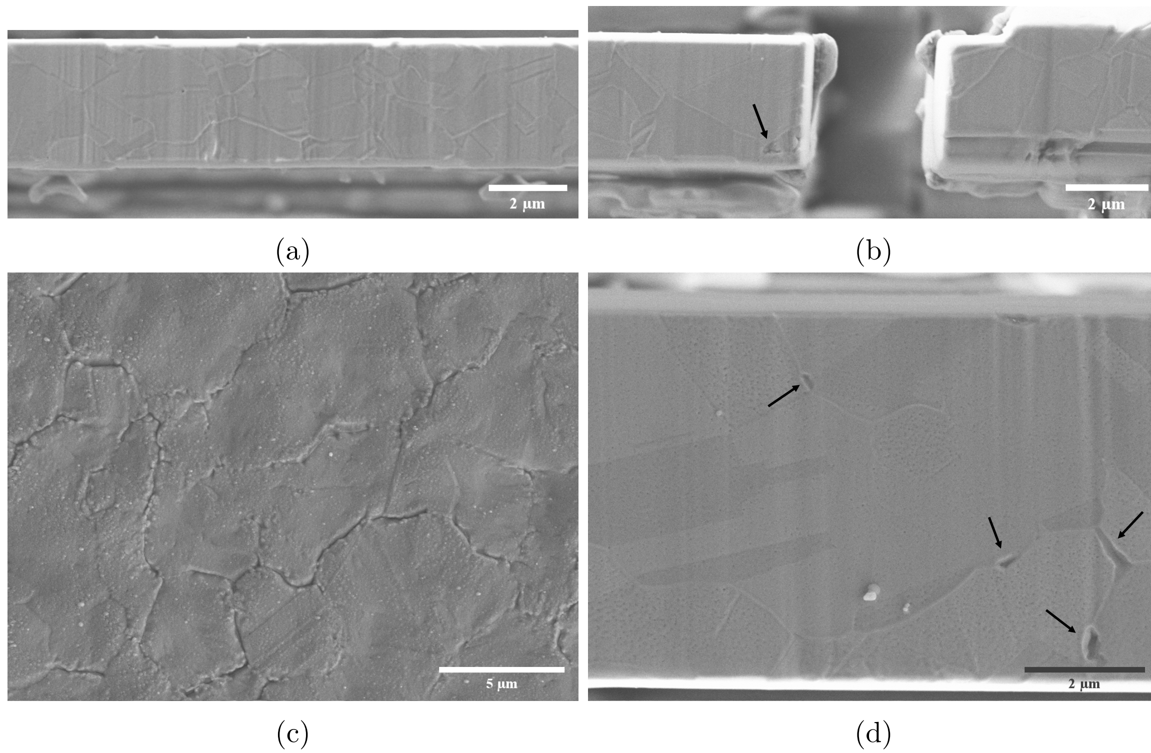

(a) (b) (c) (d)

Figure 4.9.: Examples for rounding of grain boundaries on Cu surface. Top view images of CuTiW-Notch ((a) and (b)) at 7000x magnification and CuTiW-VB ((c) and (d)) at 5000x and 12000x magnification respectively. Arrows indicate void formation at grain boundaries.

CuTiW-Notch was in cycle 2 at the maximum temperature of 350 °C. In the third cycle those extrusions increased in number and size between 325 °C and 350 °C. In the instance of CuTiW-VB-Notch, the material flow first showed in cycle 1 at maximum temperature 325 °C. The amount increased in the following cycles above a temperature of 325 °C.

The previous paragraphs covered all events observed in the Cu layer. No changes to the TiW layer could be observed. Close to the TiW-Si interface the Si layer glided outwards below the TiW layer. Examples for this behaviour can be found in figure 4.11. Silicon extrusions can be observed in every sample especially at 90° edges (figures 4.11a and 4.11b). They can also be found in the outskirts of the areas for EBSD scanning (figure 4.11c). The starting temperature seems to be around 325 °C and higher temperatures increase the amount of gliding.

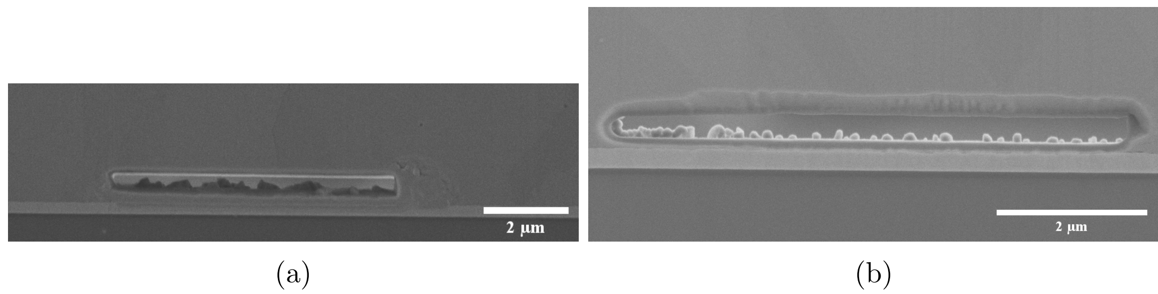

(a) (b)

Figure 4.10.: Material flow inside the notch. CuTiW-Notch (a) and CuTiW-VB-Notch (b) at 7000x and 15000x magnification respectively.

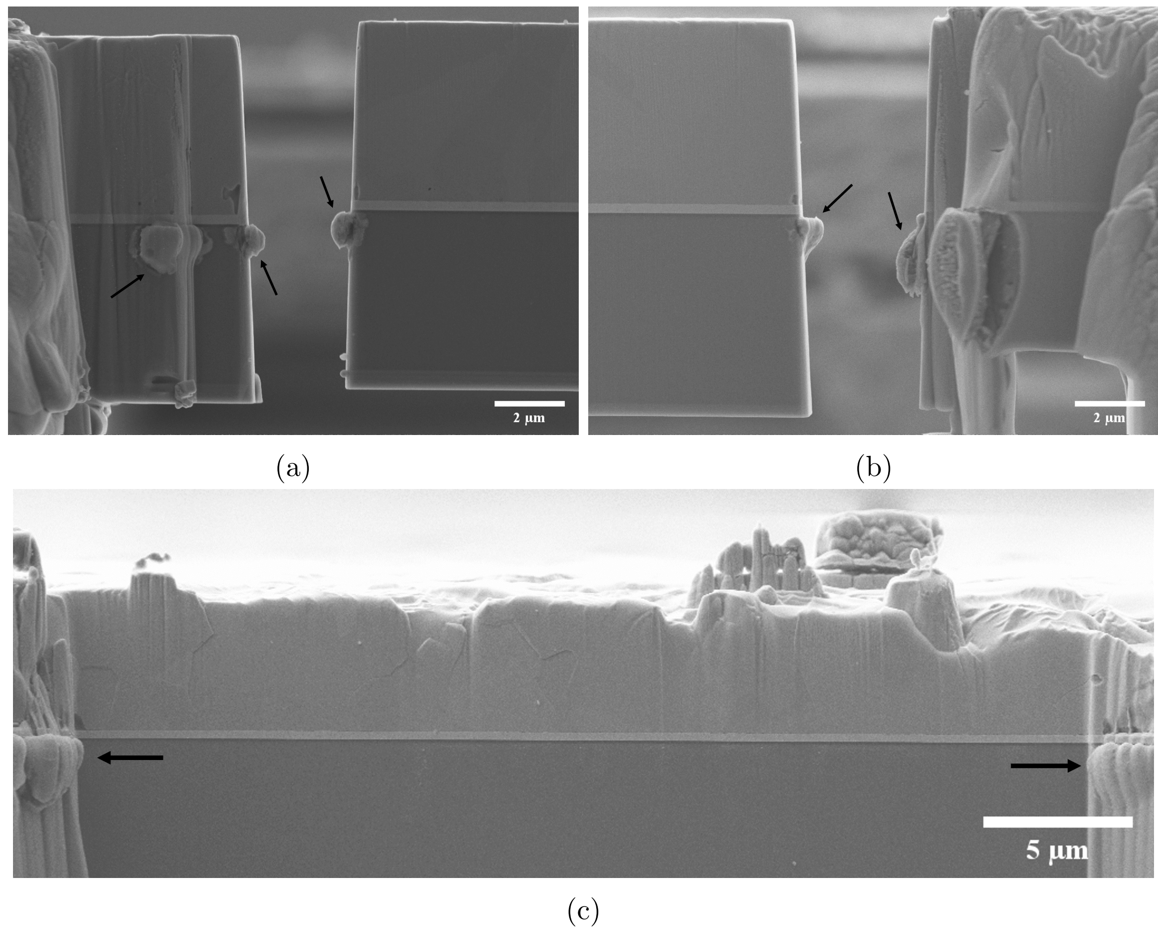

(a) (b)

(c)

Figure 4.11.: Examples for material extrusions at the Si-TiW interface. Samples CuTiW-Notch (a) and CuTiW-VB-Notch (b) at 7000x and CuTiW-VB (c) at 3000x magnification. Arrows point towards these material extrusions.

5. Discussion

The following chapter shall discuss the gathered results from the previous chapter. Special attention will be drawn towards the image processing routine, the experimental setup as well as thermo-mechanical fatigue events like microstructural changes, the resulting internal stress distribution and the absence of delamination at the Cu-TiW interface.

5.1. Image processing

As explained in chapter 2.4.1 it is essential to measure the curvature of the bent beam to calculate stresses within it. As Kirchgaßner demonstrated in his bachelor's thesis [38] overview images with a magnification of 1000x are well suited for this task. Kirchgaßner manually measured at least 60 points of the TiW-Si interface. Prior to the conducted experiments of the present work, it was assumed that the accuracy of the measurement could be enhanced by stitching six or seven SEM images with 5000x magnification. Furthermore, a Python program described in chapter 3.3 was used to avoid manually collecting the interface coordinates.
To compare the different approaches the first heating cycle of the CuTiW-C sample was evaluated four times. The results are shown in figure 5.1. Blue and orange show manually tracked coordinates of overview and stitched image, respectively. Green and red on the other hand represent the curvatures derived semiautomatically using the Python program. In 5.1a, the dashed lines indicate a linear least-squares regression performed with the SciPy package (version 1.7.1) using Python 3.8. The corresponding coefficient of determination R^2 is shown in the legend. The sum of the least squares is shown in figure 5.1b. The trends are for R^2 and the sum of least squares the same. The highest R^2 values are both produced using stitched high magnification SEM images. Both the manual tracked points as well as the automatically derived points result in fairly similar curvature values. In contrast, the deviation between slope of the 1kX processed images and the 5kX processed ones is quite evident (compare figure 5.1a). Due to faster processing and gained accuracy all curvatures were tried to be measured with stitched 5000x SEM images and the described image evaluation program using

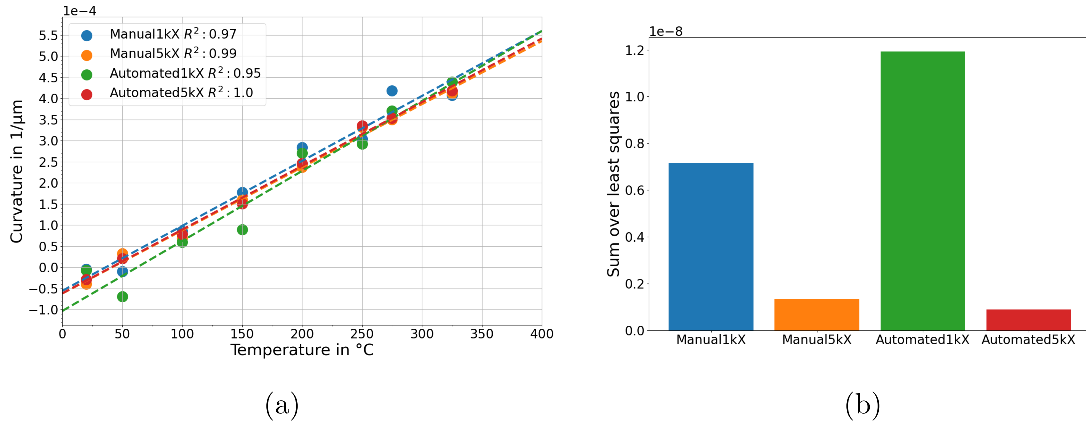

Figure 5.1.: Comparison of possible curvature measurement techniques. (a) shows the measured curvature values as well as linear fits. (b) shows the sum of the least squares yielded by fitting.

Python.

Some difficulties in the stitching and curvature measuring process and possibilities to improve the workflow shall be explained in the following. In two cases the taken high magnification images were not overlapping. Those curvatures were determined using the overview images at 1000x magnification.

Stitching with overlaps proved to be challenging as well. In the initial evaluation the author tried to automate the stitching process with several techniques. Panorama stitching is well established and can even be used on everyday technology like smartphones [51]. The present case of stitching SEM images is similar to panorama creation and even offers several possibilities for simplification. A panorama consists of multiple overlapping images taken by rotational and translational movement. This requires corrections for distortion as the final image is projected on the inside of a sphere. In the case of SEM imaging the stitching process only needs to deal with translational movement of the camera (or in this case the sample as electron beam and detector are stationary). Rotation of the single images would also be catastrophic as the measurement of the curvature would no longer be valid. ImageJ (version 1.53f [52]) offers a plugin for stitching translational only [53]. It uses the well-established technique of phase correlation and fast Fourier transforms to overlay images, followed by linear blending of the transitions. Unfortunately, the single images are seemingly to alike to be properly stitched by this method. Another technique is ORB [54] which detects keypoints in images such as edges and vertices. This was tried to be implemented using OpenCV (version 4.0.1), a Python package for image processing. Even optimizing the search area for keypoints and using the CuTiW sample with lot of debris on the front side of the beam did not lead to satisfactory results.

The temporary solution was to stitch the images manually with paint.net. A time

consuming process which should be avoided in the future. Therefore, several suggestions for improvements can be made. In the stitching process it became quite obvious, that the key features in this geometry are curtaining artefacts from FIB milling, grain boundaries and defects on the surface (compare figures 4.8 to 4.11). To align the TiW-Cu interface, it was found to be better when these defects where closer to the interface. Very clean and geometrically well-prepared samples showed more difficulties when stitching. In some cases, it was not even possible to manually stitch them. This problem could be bypassed using the overview images as templates, which is even more time consuming. Following this logic, small defects, like markers, can be introduced into the surface. This should not interfere with the mechanical response during thermal loading as those markers are small compared to the beam size. Another suggestion is intentional curtaining in the final polishing stages of sample preparation.

When it comes to taking the SEM images, there are also some points which can be improved upon. It is apparent that single images are taken with different contrast settings. Automated stitching has difficulties recognizing overlaps when they are of different contrast. There is no simple solution to this problem, but it should be possible to use an automated process which detects for example the copper phase in the image and sets the images' average brightness and contrast values to fixed values using the copper layer as a reference. Another problem is assigned to the drift of the electron beam at high temperatures, due to charging effects, which distorts the images in vertical direction. Faster scanning modes were used to solve this problem but in one case the drift was only noticed while stitching. In this case it is again necessary to fall back on the overview image.

Finally, it should be mentioned that the images were acquired with a framegrabber, which essentially takes screenshots of the SEM monitor. This implies that no metadata like stage position or contrast and brightness data is saved. The reason for framegrabbing is the inability to access the memory of the SEM computer in the given setup. Stitching might be easier if the metadata can be accessed.

After stitching the semiautomated evaluation process of the curvature follows. The ultimate goal is to automate it completely, using a SEM image as input and generating a curvature value as output. This could not be achieved, a total of seven user input parameters is needed per image. Most of them are attributed to differing brightness and contrast settings from stitched image to stitched image, which could be solved by already mentioned means. Manual locating the interface position requires at least three inputs by the user. The automated detection of the correct interface of course requires continuous brightness and contrast throughout the stitched image. Then a combination of edge detection and positional information gained from the image

from the previous temperature should enable automation. To complete this train of thought it shall be mentioned that it was tried to derive the curvature from raw, stitched images.
This can be performed by a Hough transform [55] which in this case needs to be adapted for parabolas [56]. For easier understanding it shall be shortly explained based on a linear approach. A Hough transform uses Canny edge detection to get information about direction and angle of an edge (compare 3.3). This information is used to create a 2D Hough space. For every pixel in real space a point in Hough space is created. When a line is present in real space it is represented as an accumulation of points in Hough space, which gives information about the linear equation. Hough space for parabolas is four dimensional and requires more complicated mathematical frameworks, but it is well established to use Hough transformation for parabola detection [57].
To conclude this section, it should be mentioned that the time consuming stitching and semiautomated processing is still faster compared to manual tracking and leads to correct curvature values with smaller errors due to more acquired points to fit the parabolic equation on.

5.2. Experimental setup

The derived curvature values are shown in figure 4.1. In the following section the individual samples are addressed and it is discussed which trends are observed. First some points regarding all samples are mentioned.
The setup used in these experiments uses thermocouples which are soldered to the sample holder. The distance between the solder joint and the tip of the sample is in the mm range and the sample is tested in vacuum surroundings, but nevertheless the heat loss due to thermal conduction and radiation cannot be neglected. FEA simulations show that the tip of a sample is about 15 °C colder at a temperature of 300 °C [45]. This circumstance has the qualitative effect is that data points in figure 4.1 get shifted to lower temperatures the higher the measured temperature gets. This would in theory come closer to the elastic trend at the beginning of the heating cycle. As the exact shift for each temperature is unknown this correction cannot be applied to the gathered data. This should always be considered as the plots in figure 4.1 show the temperatures measured by the thermocouples.
Another problem at high temperatures was already mentioned in section 5.1. A drift caused imaging problems, which could be avoided by higher scanning rates.
Furthermore, due to the aspect ratio of the notched samples (cross sectional area of ≈ 3.5x10 µm torsional deformation might be expected. This was not observed. Another

possible error in the curvature measurement is the tilt angle of the sample. Due to the sample holder and the sample size, correct alignment is quite challenging. The stage of the used SEM is also not able to tilt, which makes initial sample placement all the more important. However, no evident misalignment was observed during testing.

The absence of the listed possible error sources permits the conclusion, that the experiments and the curvature measurement were conducted properly and the collected data is trustworthy.

5.3. Thermo-mechanical fatigue

5.3.1. Microstructural changes

This section discusses the results described in chapter 4.3.

It was found that the Cu layer undergoes quite noticeable changes. These include voids and rounded grain boundaries, small pore development and material flow inside the notches. On the other hand, EBSD images showed rather stable microstructure, no grain growth or textural changes.

Copper has a melting point of 1357 K [58], which means 400 °C equates to a homologous temperature $T/T_m = 0.5$. This magnitude of temperature is usually sufficient to have an effect on the microstructure of copper, causing for example recrystallization processes and/or grain growth [9]. Recrystallization is not only enhanced by temperature but also by small grain sizes. The present Cu layer has a median grain size of 2.7 µm as found in preceding experiments [33]. Pure copper would undergo extreme grain growth at those temperatures having such small grains, due to secondary recrystallization [9].

In this case the stability of the grain structure can be attributed to inorganic impurities in the Cu layer [59]. During electrolytic deposition, ingredients of the electrolyte are also incorporated into the layer. During annealing (described in chapter 2.3) these impurities diffuse towards the grain boundaries and decrease the grain boundary mobility at elevated temperatures. Bigl et al. showed that these impurities are mostly Cl and S and their contents are in the 100 ppm range [25]. He compared the Cu film used in the present thesis with a purer Cu layer of similar initial grain size. The latter experienced significant grain growth in a cyclic thermo-mechanical experiment with $T_{max} = 400$ °C. While the first film did not experience any textural changes, the second one showed an increase in (100) orientation enabled by twin boundary migration. During nanoindentation testing it was also shown that the inorganic impurities increase the hardness at twin and grain boundaries, indicating higher necessary stresses to plastically deform them [34].

Interestingly Bigl et al. [19] also demonstrated in another study that the substrate thickness has an influence on grain growth. Regarding the herein presented work this would imply that the grain growth should differ significantly between the beam (Si thickness only around 4 µm) and the area for EBSD images (Substrate with the original thickness of 725 µm). However, it was shown that in no case grain growth was observed. Bigl changed the substrate thickness between 725 and 220 µm, so it is only possible to approximate from 220 µm to the beam geometry. He suggests that the increased curvature values with decreasing substrate thickness fatigue the material faster, enabling grain boundary movement. The first indication for grain growth is at 100 cycles, which indicates that three cycles are simply not enough to degrade the material in a low cycle fatigue kind of manner.

In another study, Wurster et al. [26] investigated an impure and a pure Cu film. It was again shown that S and Cl at the grain boundaries prevented grain growth and texture changes. As Wurster used a higher heating rate and therefore strain rate it can be concluded that higher strain rates enhance the velocity of microstructural changes. As the herein presented experiments have heating cycles in the 120 to 150 min range, this poses another reason why no grain growth and texture changes were observed.

While the grain and twin structure is stable during testing, void formation was observed at temperatures above 325 °C especially at grain boundaries and the Cu-TiW interface (compare figure 4.8). This correlates with experiments performed in literature [19, 36] as well as proposed models [3, 22, 60]. It was found in previous studies that the formation of these voids can be linked to inorganic impurities, too [25]. As barrier for void formation the free energy ΔG has to be overcome.

$$\Delta G = \frac{4\gamma_i^3 f_v}{\sigma^2} \tag{5.1}$$

The interfacial energy γ_i, a geometrical factor f_v as well as the locally applied stress influence ΔG. Assuming that the Cu-TiW interface, like grain boundaries, is a favourable location for impurities, it is understandable that voids are forming at grain boundaries and interfaces due to a reduced γ_i, induced by impurities, which scales to the power of three. Additionally, the stresses in the copper layer are maximum at the Cu-TiW interface. Kleinbichler et al. [36] used images of the copper surface to define two stadiums of degradation regarding voids. Nucleation and growth. As long as voids are small, they do not interact with each other, but as soon as they connect, larger networks are forming. As these networks are not detected, it is concluded that more heating cycles would be necessary to reach void coalescence stages.

Figure 4.8a shows the opposing stump of the beam. During thermal cycling void formation was noticed and detail images were taken. In figure 5.2 an unheated image

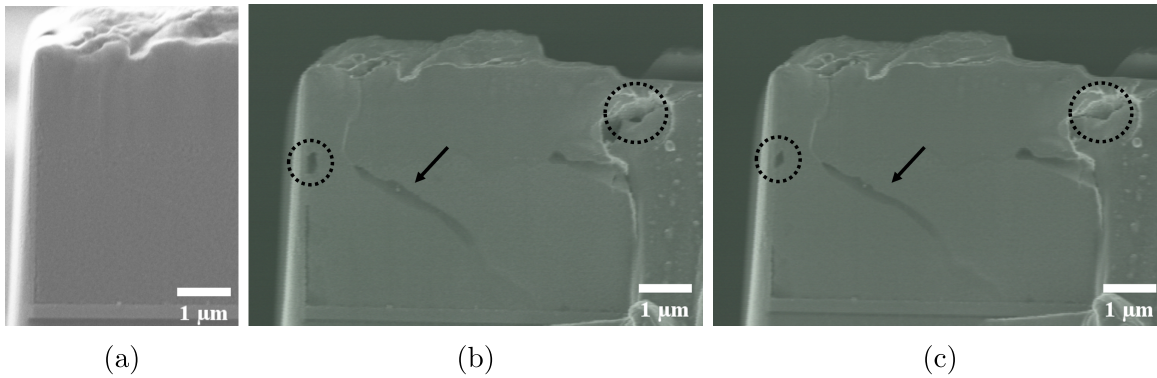

(a) (b) (c)

Figure 5.2.: Void growth stages. Sample CuTiW-VB preheating (a) at 7000x and after cycle two (b) and cycle three (c) at 10000x magnification respectively. Larger pores (arrow) seem to stay at their size between cycle two and three while smaller ones (dotted circles) continue growing.

(a) is shown as well as images after cycle two (b) and three (c). During the experiments, the formation was not noticed prior to the beginning of cycle three, but using the in-situ images of cycle one, the onset of void formation in this area can be set to 325 °C. Comparing figures 5.2b and 5.2c shows that large voids seem to stay around the same size, while smaller ones grow quite significantly in between cycles.

It should also be mentioned that samples undergoing the vacuum break during deposition seem more prone to void formation. As the vacuum break is only connected to the Cu-TiW interface being decorated with TiO_x and WO_x [7], and void formation is linked to impurities stemming from the electrolyte, this circumstance lacks causality. As post experiment SEM images were only taken for the CuTiW-Notch sample and the VB samples two reasons for the lack of observed voids in CuTiW and CuTiW-Notch can be given. CuTiW-Notch was heated only to 350 °C in two cycles. The VB samples exceeded these temperatures or as in the case of CuTiW-VB 400 °C could be reached in all three cycles. As the onset of void formation was set around 325 °C insufficient heating may be one reason. Another explanation might be that void formation is randomly distributed and the observed area was too small to provide statistical valid information.

In his thesis Kirchgaßner also observed void formation. In his case they were of larger size and quantity. As the samples in this work are heated to higher temperatures more often (maximum of 400 °C in three cycles instead of Kirchgaßners 350 °C in two cycles) void formation does not seem to depend on thermal activation only. Stress gradients are supporting vacancy diffusion which leads to void formation. In thinner films, these stress gradients are steeper and the Cu layer of Kirchgaßner is only 40 % of the thickness used in the samples herein. Accordingly, his sample shows larger and more voids. In chapter 5.3.4 the stress gradient and its effects are further discussed.

Another interesting phenomenon is that no beam showed pore growth on the monitored surface, while the top and the stumps show a significant amount. The accumulation of voids on the top of the beam might be explained by the fact that this is the region with the least restriction to expand during heating as Si and TiW have lower α. Therefore, it is easier for vacancies to diffuse and accumulate to voids.

In principle the discussed void networks are microcracks inside the Cu layer leading to a decreased functionality and structural integrity. Wimmer et al. [30, 33] documented embrittling grain boundaries at $T > 200\,^{\circ}\mathrm{C}$ in tensile experiments due to the before mentioned inorganic impurities. This further contributes to the failure of the copper film during thermal cycling [35, 61]. Finite Element Models also indicate that voids on their own can act as crack nucleation sites, demonstrating their impact on the fatigue of the material system [3, 22, 60].

Figure 4.9c shows the unprepared copper surface from sample CuTiW-VB. One can see that due to thermal activation (reduction of surface energy [9]) grain boundaries are rounded. This is another indication of onsetting fatigue as also documented by Hoffmann et al. [37]. Similar behaviour can be observed on top of all samples. Figure 4.9d depicts for example grain boundaries which are sliding against each other (detail b).

A further microstructural change observed after experiment is the formation of mini-pores. These can be seen in figures 4.8a, 4.8b and 4.9d. No specific temperature or time point of first occurrence can be found, as these features are only observed in high resolution images. Furthermore, most of the pores formed on top of the beam instead of the in-situ monitored front surface. It is not known to the author how these pores originate, as there is no sound explanation why they are forming only on the top but not the front. It was observed however that in some locations the size and amount of pores seems to be dependent on the microstructure (compare figure 5.3). Also, they formed only on sample CuTiW-VB, which is the only sample to be heated three times to 400 °C. It is encouraged to investigate this feature in future works, as it is excluded from the coverage of the present work.

No change to the TiW layer was observed during testing. Kalha et al. [7, 62] suggest that at 400 °C Ti is segregating to the surface of the film. It is out of the scope of this thesis to confirm that or investigate the influence of the copper layer on this behaviour. However, the performed experiments coincide with Kalha to the extent that the TiW layer is not fatigued.

Regarding the Si layer, a characteristic push out of material can be observed at the Si-TiW interface. This was already reported by Kirchgaßner in his thesis [38], where he referred to this phenomenon as terraces. It can be assumed that the phenomenon

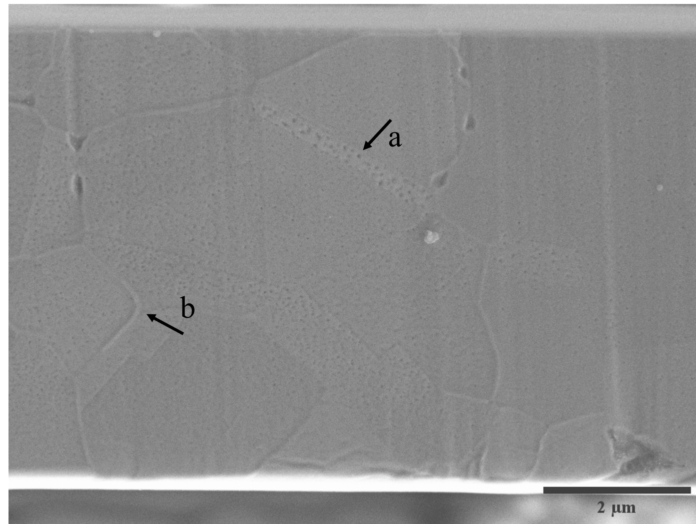

Figure 5.3.: Detail image (12000x magnification) of small pore formation and sliding grain boundaries. On the top of sample CuTiW-VB it can be seen that the amount and size of the pores depends on the microstructure below (maximum in detail a). Detail b shows an example of sliding grain boundaries.

observed here is not related to delamination but rather to stress induced diffusion at elevated temperatures.

5.3.2. Curvature measurements

During the next paragraphs, the experimentally measured curvature values are compared to results provided by the FEA model and previous experiments. Some influences regarding experimental setup and sample geometry are listed and discussed.
The expected behaviour of the samples can be briefly summarized. The initial curvature is a result of the residual stresses in the respective layers. Upon heating the curvature increases linear (compare Hsuehs' model) until a temperature is reached, at which the Cu layer will start to deform plastically and the curvature value will plateau or at least not increase with the same rate as in the linear regime. After cooling, the plastic deformation has relaxed the residual stresses in the Cu layer, while the quasi-elastic TiW layer is unchanged stress-wise. Additionally, microstructural changes due to fatigue mechanisms change the properties of the Cu layer and thus the room temperature curvature is different. The next heating cycles exhibit a larger amount of elastic response, as hardening in the Cu layer took place during earlier cycles. From now on only microstructural changes influence the curvature response. Kirchgaßner could also observe this behaviour during his experiments [38].
The same can be said about sample CuTiW. The initial curvature is about $0.7 \times 10^{-4}\, ^{1}/_{\mu m}$ which indicates net compressive residual stresses in the film structure. The substrate itself is stress free as was discovered via ion beam layer removal experiments

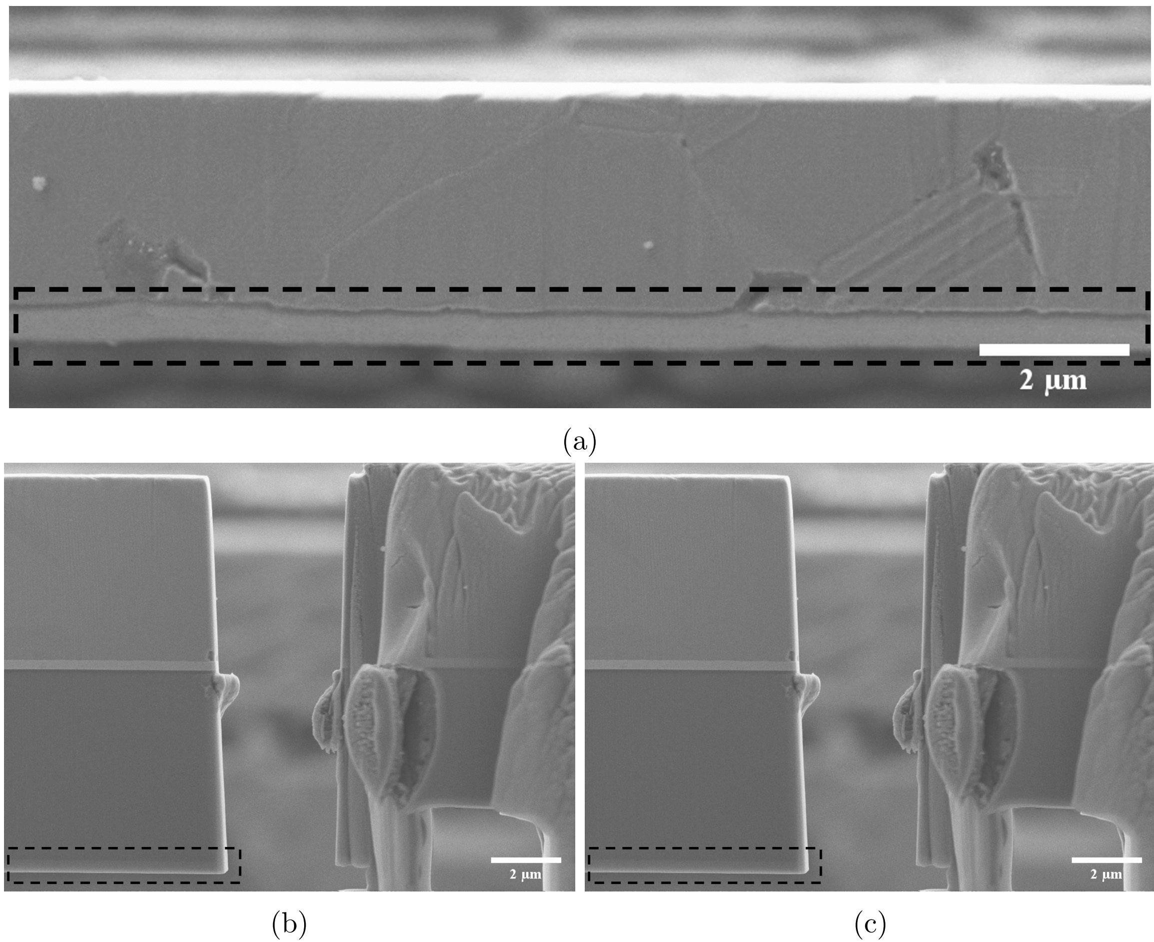

Figure 5.4.: Redeposition (dashed rectangles) during EBSD area preparation on CuTiW-VB-Notch, (a) and (b), and CuTiW-Notch (c). All images are taken at 7000x magnification. The bottom of (a) shows the backside of the beam.

[47, 63, 64]. This is valid for all samples. Up to 200 °C the experimental data shows a linear trend, similar to Hsuehs' model and in close correlation to the FEA data. The first cycle ends at 275 °C. As cycle one deviates only little from the elastic behavior it is reasonable that cycle two starts with a similar curvature like the first one. Again, a linear trend is observed, now up to 300 °C, at which point the curvature is plateauing around 7×10^{-4} 1/µm until reaching 400 °C. The third cycle starts with a significant reduction in curvature, indicating relaxation processes as well as plastification of the copper layer, which was reported by Kirchgaßner as well. The curvature exhibits a linear increase up to 400 °C where the value again is slightly above 7×10^{-4} 1/µm, hinting towards a fully elastic response after the relaxation in cycle two.

However, the other samples show a different behaviour. First the maximum curvatures reached are smaller than in CuTiW (4.5×10^{-4} 1/µm compared to 7×10^{-4} 1/µm), which can be explained by the sample geometry, as the FEA model and the elastic model of Hsueh also do not reach as high values as in the case of CuTiW. Second the initial

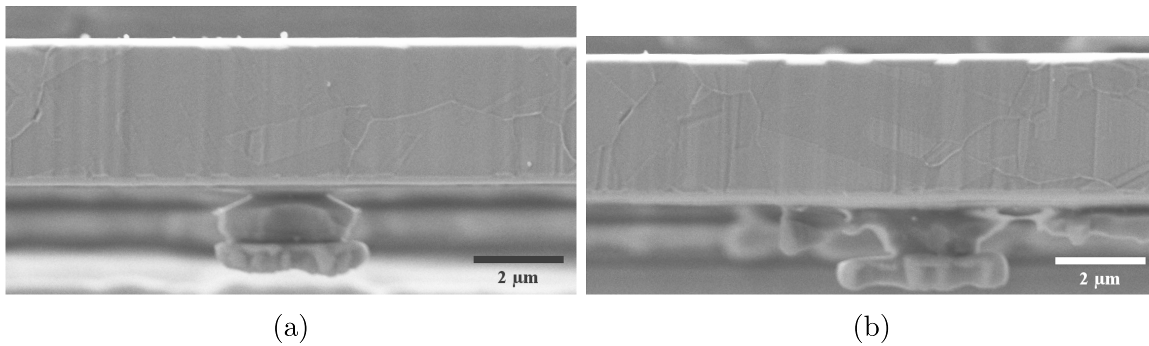

(a) (b)

Figure 5.5.: Unfinished sample preparation of the backside (CuTiW-Notch). Both images taken with 7000x magnification.

curvature is closer to zero and does not change in between the heating cycles. This is in correlation with Kirchgaßners experiments. The curvature plateaus above 300 °C which can for example be seen in CuTiW-VB-Notch. Returning to room temperature the curvature is not significant different from the initial curvature. The exception is sample CuTiW-VB, which acts similar to CuTiW, reducing its initial curvature to zero.

It can be assumed that the residual stresses in the Cu layer are reduced. The reason why no change in room temperature curvature between cycles is observed may be found in an inaccurate sample preparation. Figure 5.4 shows examples for redeposition during FIB milling when the EBSD area was prepared (dashed rectangles). The back as well as the bottom of the beam are covered with a up to 500 nm thick layer of undefined material. The front was polished after redeposition and prior to testing. The notched samples are especially thin and thus this inaccurate sample preparation might have a significant influence, constraining the material stack from deforming freely. The unnotched samples both are free of redeposition as they were fabricated after the EBSD area.

A similar incident can be found on the backside of CuTiW-Notch. In FIB contrast the backside seemed finished, but in SEM it is clearly visible that a few features of Si remain. Examples are shown in figures 4.9a, 4.9b and 5.5. It can be assumed that this has no significant influence on the behaviour of the beam, as the features do not constrain any layer from expanding or contracting normally during heating. The same can be said about the debris on the front of CuTiW (compare figure 4.5a).

5.3.3. Modelling of internal stresses

One goal of the presented work is to get an understanding about the internal stress distribution caused by the α mismatch and the plastification of the Cu layer. Two models were proposed during this thesis. On the one hand a FEA model (refer to

3.4) and on the other an analytical approach which is solved with help of the Newton method. In the following benefits and drawbacks of the analytical model are discussed, including a comparison with the FEA model.

In order to visualize the stresses between heating cycles, figures 5.6 and 5.7 show the internal stress distributions derived by the analytical and the FEA model, respectively. As an example, the plots for sample CuTiW-VB-Notch are shown. The distributions are similar for other samples, which is why only one sample is displayed here. The others can be seen in appendix B.

However, there is one exception, this being CuTiW-VB. Using the curvature and temperature of the first cycle, the analytical model is not converging with the Newton method. It is unknown to the author as to why this is. A hypothesis is that the bilinear hardening model is not suited for the case when the whole Cu layer is plastically deformed, which would be the case at 400 °C in cycle one. Yet it is possible to circumvent this problem as the equation system has a solution for zero. A custom zero solution algorithm would be capable of solving the model. The implementation is however out of the scope of this thesis.

It was already stated in section 4.2 that the main points in both models are generally the same. Comparing figures 5.6 and 5.7 one can spot some differences. Again, the elastic region (top) and Without an optimizing algorithm the FEA model starts with $\kappa = 0\,{}^{1}/_{\mu m}$. This is not true, as the TiW layer has quite significant residual stresses and in figure 5.7a it can be seen that $\Sigma F = 0$ is not fulfilled. Comparing to figure 5.6a shows that the analytical model is able to adjust for the initial curvature and always fulfills $\Sigma F = 0$.

After heating to the first maximum temperature the differences are less obvious. Due to the curvature the stress gradient within the layers is steeper (in the images the slope decreases, as the stress gradient is inverse proportional to the portrayed slope). The stresses in the TiW layer relax elastically (400 MPa in the analytical model, 600 MPa in the FEA model). The most interesting layer is the Cu layer: Due to the bilinear hardening model the border between elastic and plastic deformation is quite evident in the analytical model. The FEA model provides a smoother stress deviation in the Cu layer, but the trend is similar. With later cycles, the maximum temperature increases (compare table 4.1) and thus the portion of the plastically deformed layer.

Both models provide information about the accumulated plastic strain in the Cu layer. This is shown in figures 5.6h and 5.7h. Again, the models show the same trends, an approximately 1 µm thick undeformed top layer, as well as increasing plastic strain towards the Cu-TiW interface. The absolute value is larger in the FEA model, but it is the same order of magnitude for the analytical model. In the middle of the Cu

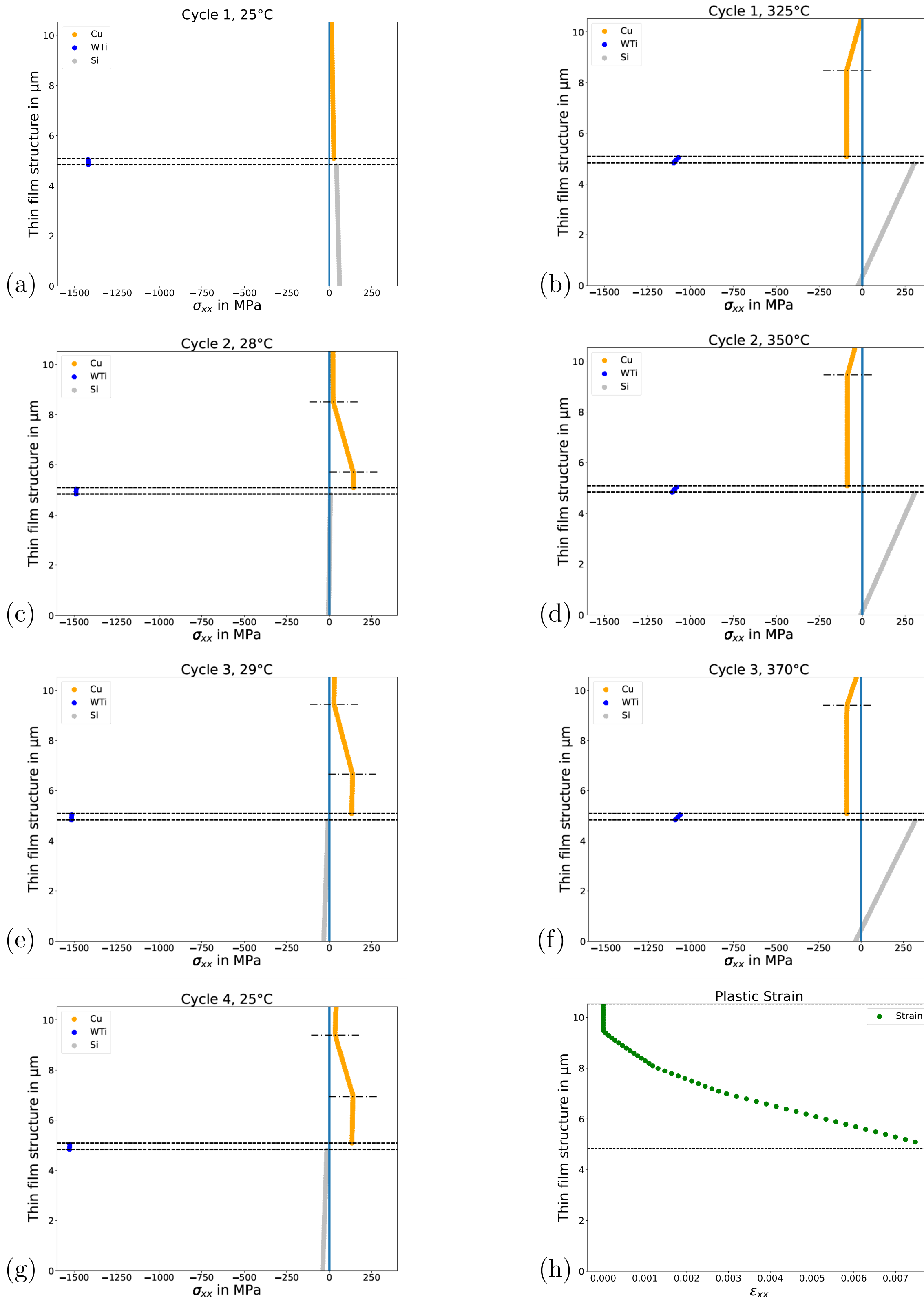

Figure 5.6.: Analytical model of CuTiW-VB-Notch. Rows correspond to the cycles and columns to low temperature and maximum temperature. In (h) the total accumulated plastic strain after all cycles is shown. The dash dotted lines divide the elastic (top) region, the region plastically deformed below maximum residual stress (middle) and the region deformed to maximum residual stress (bottom) in case of the low temperatures, in case of high temperatures it divides elastic (top) and plastic (bottom) regions.

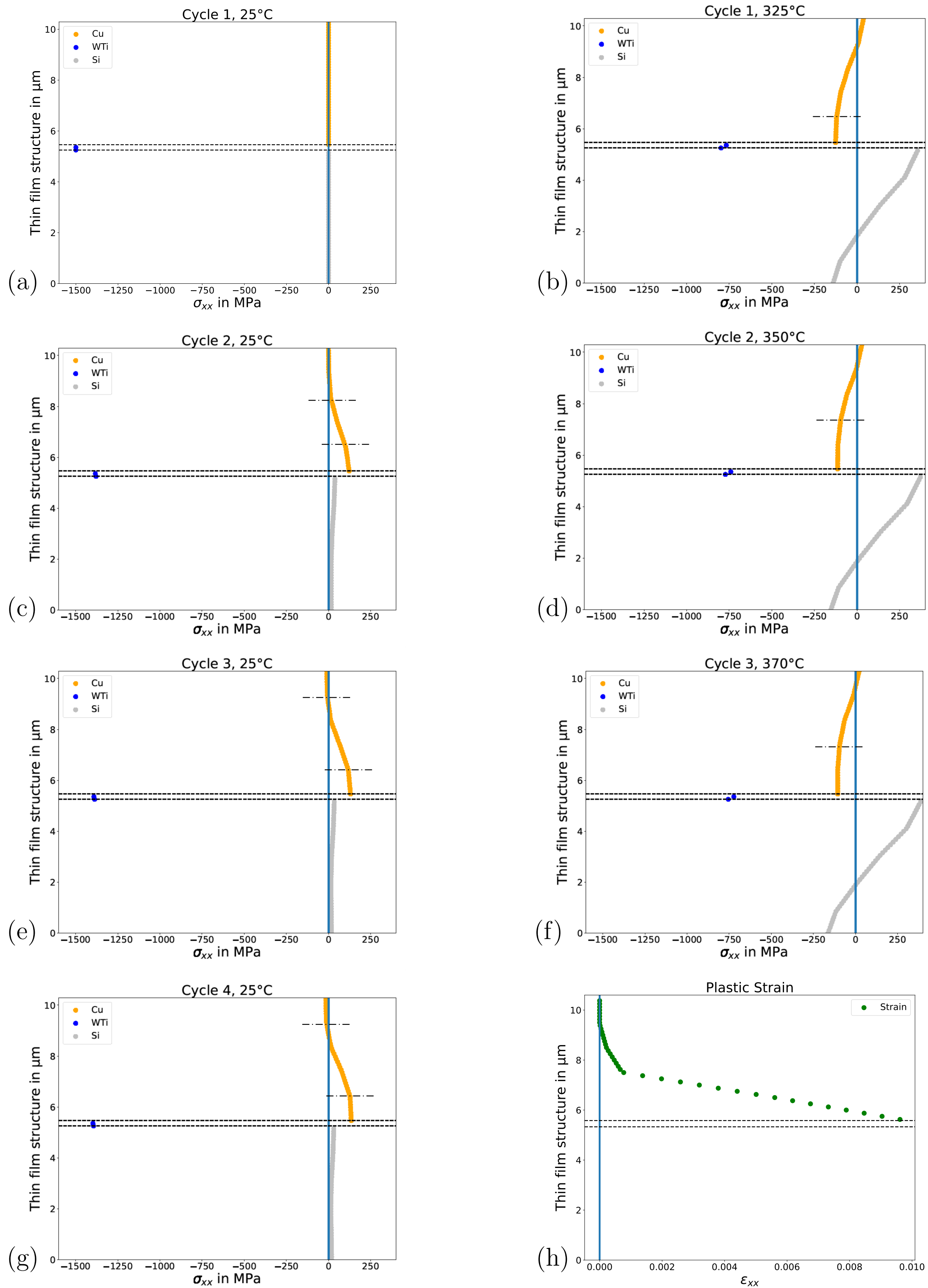

Figure 5.7.: FEA model of CuTiW-VB-Notch. Rows correspond to the cycles and columns to low temperature and maximum temperature. In (h) the total accumulated plastic strain after all cycles is shown. The dash dotted lines divide the elastic (top) region, the region plastically deformed below maximum residual stress (middle) and the region deformed to maximum residual stress (bottom) in case of the low temperatures, in case of high temperatures it divides elastic (top) and plastic (bottom) regions.

layer, the FEA model predicts less plastic deformation. Still, the general trends and the order of magnitude are well described by the analytical model.

The same can be said about the other notched sample (CuTiW-Notch, see appendix B). In contrast, the analytical model predicts similar plastic strains for the unnotched samples, while the FEA model shows less plastic strain (for example CuTiW, maximum 7 % in the analytical model and 1.8 % in the FEA model). This is an indication for the influence of the sample width, which is not considered by the analytical approach. This still encourages the proposal to accept the analytical model. It seems that even bigger simplifications like a uniaxial approach and the bilinear hardening model for the Cu layer have no negative effect on produced trends. For absolute values regarding plastic strain more detailed investigations would be necessary, like FEA models considering the three-dimensional nature of the sample.

However, there are a couple of drawbacks regarding both models. The initial residual stresses in Cu and Si were regarded to be zero. This is not entirely true, as the production route of the wafer entails the deposition of TiW and the following cooling to room temperature induces compressive stresses of −1.5 GPa in the TiW layer [23]. These stresses must be countered by the Si layer. For simplicity it is assumed that the residual stresses are distributed evenly throughout all layers. Then it can be calculated that a 250 nm thick film of TiW induces an average of 0.5 MPa in the 725 µm Si substrate. Thus, the assumption of a stress free substrate is applicable and in correlation with results using the ion beam layer removal method [47, 63, 64].

The residual stresses of Cu were also not known prior experiment. Chen et al. presented an ion beam layer removal experiment with a similar material architecture as investigated in this thesis [63]. They found significant tensile stresses of 200 MPa in a 400 nm Cu layer. In the case of 5 µm Cu material used herein this stress would equal 16 MPa. which is around a tenth of stress needed for plastification at room temperature. It may not have a huge influence on the outcome of the models, but it should be considered in follow up experiments. It was already explained that with the used experimental setup the residual stresses of the thin film layers cannot be estimated. It is referred to appendix A, where an alternative experimental setup is proposed. A different approach would be to add an ion beam layer removal experiment to the workflow. This would not only give information about the magnitude of the residual stresses, but also fluctuations within the layers and across the interfaces.

5.3.4. Delamination

The reason why two samples have been notched at the Cu-TiW interface is to cause delamination. In chapter 5.3.1 it was explained that previous studies suggested thermo-

mechanical fatigue is the reason for voids being generated, which accumulate to networks acting as microcracks. Experimental results and simulations indicate that these cracks initiate at the interface, especially at convex features [3, 22]. The cracks were observed to propagate perpendicular to the interface into the copper layer. Adding notches at the interface it was assumed that these would act as crack nucleation sites, even at early fatigue stages.

As described in 4.3 no cracking is observed. In the following paragraphs it shall be discussed, what signs of fatigue in the notch area might indicate future delamination and how the stress state at the interface could be converted to a stress intensity factor, implying spontaneous delamination failure.

First the notch positioning in vertical direction of the material stack shall be addressed as well as difficulties encountered with notch fabrication. In figure 4.10 it can be seen that in the case of CuTiW-VB-Notch the notch is quite successful positioned at the interface. However, due to redeposition around the notch, it is challenging to align the notch perfectly. This is experienced in sample CuTiW-Notch, where remainders of redepositioned material around the notch can be seen, resulting in a 300 nm offset from the interface. As no delamination is observed in either sample, it is difficult to estimate the influence of this misalignment.

Nonetheless a trend is observed, which indicates that this misalignment does not matter too much. It is again referred to figure 4.10. In both samples material flow inside the notch is observed. Interestingly these extrusions occur solely on the side closer to the interface. The difference between both samples is, that CuTiW-Notch, the notch being offset, experiences more severe extrusions, which can be explained, as more Cu is below the notch.

It is assumed that these extrusions stem from a mechanism called Kirkendall effect [65]. Diffusion of vacancies towards vacancy sinks, like interfaces or grain boundaries, lead to material transport in the opposite direction, which is often the surface of the material, resulting in extrusions. This effect can also be observed to a smaller scale on the surface of the beam (figure 4.8c). The severe extrusions in figure 4.10a indicate a significant amount of void formation at the interface. This may be explained by higher stress gradients in the thin Cu layer between interface and notch compared to the 5 µm layer of Cu in the rest of the beam. Secondly, the diffusion paths for the vacancies are shorter below the notch, compared to the entire Cu layer thickness. A higher driving force, due to higher stresses combined with a shorter diffusion path result in a faster material transport, and therefore in a significant amount of extrusions in the notch. As the material is coming from the interface, void formation and delamination after a higher number of cycles can be expected.

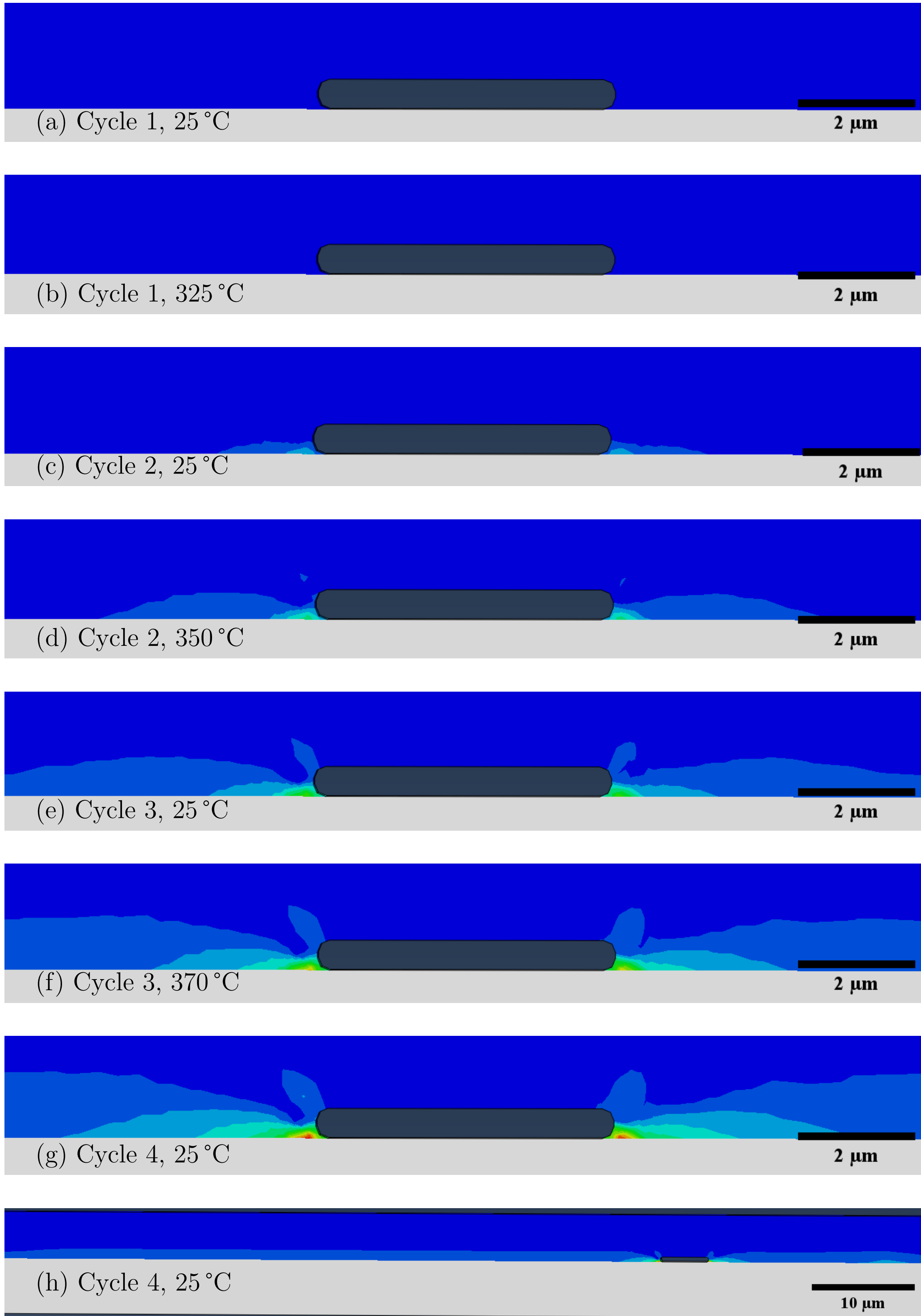

Figure 5.8.: The accumulated equivalent plastic strain PEEQ in CuTiW-VB-Notch. The corresponding color legend is shown in figure 5.9. (a) to (g) show the area around the notch during cycling, (h) shows the entire beam.

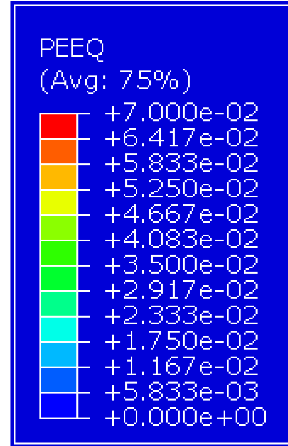

Figure 5.9.: Legend for figure 5.8.

In addition to this train of thought, the FEA model provides further indication towards later delamination. In figure 5.8 the accumulated plastic strain PEEQ is shown in the area around the notch during the heating cycles. The corresponding legend is shown in figure 5.9. As in other simulations it can be seen that the maximum plastic strains are located at the convex notch rounding reaching away from the notch [3, 22]. The highest plastic strain is located at the interface and it is around seven times larger than at the interface without notch (7 % compared to 1 % plastic strain after the experiment). The rest of the beam has a very even strain distribution (compare figure 5.8h). From a strain-based fatigue point of view the chosen position of the notch was quite promising, but further investigations (experiments or simulations) could alter the horizontal notch positioning, to increase the ratio of maximum strain to base level strain in the rest of the beam.

Another information which can be derived from figure 5.8a to 5.8g is that plastic deformation accumulates during loading as well as unloading. This further promotes the conclusion, that the initial assumptions made carrying the analytical model are indeed correct.

Material failure can occur in two ways, one being the described fatigue route, where small, recurring loads lead to microstructure degradation and failure. The other possibility is spontaneous crack extension at the interface due to critical loading. This was not achieved during experiment, but the analytical model provides an estimation for the stress mismatch $\Delta\sigma$ between the TiW and the Cu layer. In table 4.2 K_{II} values can be found, corresponding to internal stresses and sample geometry. First it can be stated that the largest values appear after one heating cycle at room temperature. After cycle one, no significant changes are observed and at high temperatures smaller K_{II} is measured.

The observed maximum stress intensity is around $K_{II} = 2.7\,\mathrm{MPa}\sqrt{\mathrm{m}}$. Critical frac-

ture toughness values of metals are usually above $10\,\mathrm{MPa}\sqrt{\mathrm{m}}$ and copper reaches even $100\,\mathrm{MPa}\sqrt{\mathrm{m}}$ as it is a very ductile material [66]. As the measured K_{II} is very small compared to critical fracture toughness, it is not surprising that no spontaneous delamination occurred. However, these values should be taken with a grain of salt, as they are based on simplifications explained in section 4.2. For ductile materials there is however an approximation, which is called the J-Integral J. J is the ductile equivalent to the energy release rate per crack elongation. In a plane stress configuration it is related to K following equation (5.2):

$$J = \frac{K^2}{E} \tag{5.2}$$

The deviation from linear elastic fracture mechanics and the implementation of bimaterial cracking was investigated by Alfreider et al. [27, 29]. In recent micro-cantilever bending experiments they measured J of the Cu-TiW interface. Using equation (5.2) the derived K_{II} values can be converted to J using $E_{Cu} = 110\,\mathrm{GPa}$.

$$J = \frac{(2.7\,\mathrm{MPa}\sqrt{\mathrm{m}})^2}{110\,\mathrm{GPa}} = 66.3\,\frac{\mathrm{J}}{\mathrm{m}^2} \tag{5.3}$$

This value lies below the value of crack extension onset found by Alfreider ($J = 74.3\,\frac{\mathrm{J}}{\mathrm{m}^2}$). This value is only true for the VB samples, as the oxide layer between Cu and TiW encourages a more brittle failure at the interface. Samples without vacuum break were deformed plastically without crack extension.

Nevertheless, the calculated J value in this work is smaller than the produced values by Alfreider which shows that the stress mismatch at the interface is not large enough to induce delamination. This is also observed in the post experiment SEM images.

Considering equation (4.1) the horizontal position of the notch shall shortly be discussed. Moving the notch towards the end of the tip approximately doubles the geometry factor $F(a/b)$. As K is squared to derive J the resulting J-integral values could be potentially quadrupled to around $230\,\frac{\mathrm{J}}{\mathrm{m}^2}$. This value is in the order of magnitude where Alfreider observed visible crack extension on samples which experienced vacuum break. Therefore, an altered notch position might be worth investigating in future experiments.

6. Conclusion

In the present work thermo-mechanical cyclic experiments were conducted on a thin film structure, including a Cu layer, commonly used in microelectronics. During three heating cycles to maximum temperatures of 400 °C in-situ images were taken to measure the curvature of a beam prepared by FIB milling. Using curvature and temperature a bilayer elastic internal stress model was adapted to a three-layer model capable of incorporating known residual stresses and plastic deformation. To verify the findings a FEA model was simulated.

A semiautomatic image processing routine was implemented with great success to accelerate the curvature measurement. This route enables evaluations at higher resolutions within shorter time spans, compared to manual interface tracking.

Regarding the image processing software further improvements towards automation should be undertaken. After this experiment a database of images and curvatures can be created enabling integration of machine learning in the interface detection procedure.

No grain growth or orientation change within the grains was observed during heating. This can be attributed to the inorganic impurities originating from the electrolytic deposition process of the Cu layer as they have a pinning effect on the grain boundaries.

During the experiments severe changes to the microstructure of the Cu layer were observed, indicating plastic deformation. These included void formation at grain boundaries and the Cu-TiW interface, which was also linked to the inorganic impurities in the Cu layer as they lower the interfacial energy. Another influence on the amount and size of voids was explained by the sample geometry as steeper stress gradients in thinner films encourage the diffusion of vacancies.

Two samples were notched to increase the chance of delamination of the Cu layer. It was discussed both from a mismatch stress induced fracture point of view as well as a plastic strain induced fatigue why no delamination occurred during experiment. When positioning the notch towards the end of the beam an increased stress intensity could lead to spontaneous delamination during cooling. The conducted FEA simulation showed however that large plastic strains were already building up at the notch which agrees with the material extrusions observed in the notch area. Therefore, it can be

said that more heating cycles as well as higher heating and cooling rates lead to more fatigue, which might lead to a delamination of the Cu and TiW layer.
In order to circumvent complicated FEA simulations in the future, an analytical model was proposed to calculate internal stress distributions within the layers. It was achieved to include known residual stresses of the TiW layer as well as predicting plastification in the Cu layer, using experimental data. The stress distributions and the amount of accumulated plastic strain is in close agreement with the conducted FEA model. When the sample width is not small compared to its height, the amount of plastic strain is overestimated but the general trend is correctly predicted by the analytical model. Unfortunately, it is not possible to derive unknown residual stresses from the model. Thus, an adapted experimental setup is proposed in the appendices to acquire those as well. The model is adjustable to any thin film architecture and is also applicable to structures with more than three layers.
To reach delamination in future experiments the following suggestions can be made.

- The strain will accumulate further during more cycles of heating, therefore adding more cycles is a time intensive but easy solution.
- If stress induced delamination is investigated the notch position should be closer to the beam tip.
- Heating directly to maximum temperature increases the strain rate significantly, inducing more plastic damage in the process. The alternative is an ex-situ setup which is capable of faster heating rates.
- Reducing the Cu layer thickness increases stress gradients and enhances microstructural defect formation.

A. Alternate experimental setup

Instead of one beam per sample, two beams should be prepared. One being the same as in the conducted experiments and one stripped of its top layer.
The proposed experimental setup enables the measurement of residual stresses as well as plastic fatigue during thermal cycling. It applies to any layer architecture but for convenience the structure investigated in this thesis is used.
First one has to consider an elastic bilayer model with the Cu layer removed.

$$\sigma_{xx,1}(z) = E_1 \left[\left(z - {}^{h_1}\!/_2\right) \kappa + \epsilon_1 \right] \tag{A.1a}$$

$$\sigma_{xx,2}(z) = E_2 \left[\left(z - \left(h_1 + {}^{h_2}\!/_2\right)\right) \kappa + \epsilon_2 \right] + \sigma_{r,2} \tag{A.1b}$$

$\sigma_{r,i}$ is the residual stress in layer i. The Si layer shows no residual stresses as found in earlier experiments [47, 63, 64]. There is a constraint regarding strain continuity.

$$\epsilon_{xx,1}(z = h_1) = \epsilon_{xx,2}(z = h_1) \tag{A.2}$$

with

$$\epsilon_{xx,1}(z) = \left(z - {}^{h_1}\!/_2\right) \kappa + \epsilon_1 + \alpha_1 \Delta T \tag{A.3a}$$

$$\epsilon_{xx,2}(z) = \left(z - \left(h_1 + {}^{h_2}\!/_2\right)\right) \kappa + \epsilon_2 + \alpha_2 \Delta T \tag{A.3b}$$

As the beam is in a force equilibrium the following equation is zero.

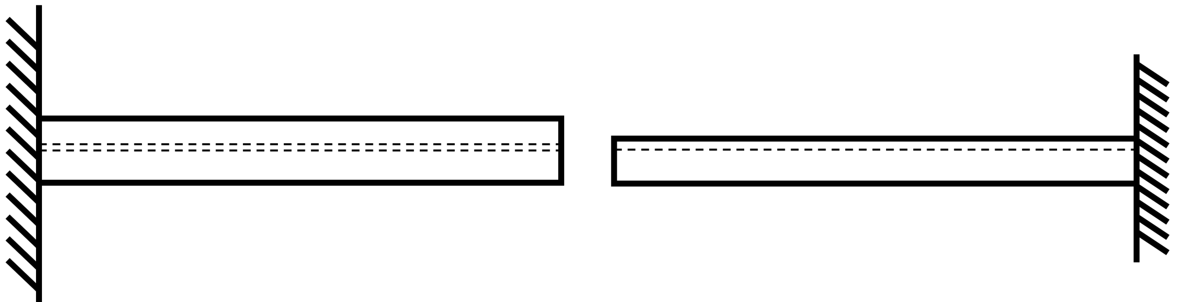

Figure A.1.: Proposal of simultaneous bi- and trilayer experiment

$$\Sigma F = 0 = E_1 h_1 \epsilon_1 + h_2 \left(E_2 \epsilon_2 + \sigma_{r,2}\right) \tag{A.4}$$

Equations (A.1a) and (A.1b), (A.2) and (A.4) yield four equations for five unknowns, therefore $\sigma_{r,2}$ can be determined iteratively. If one of the layers deforms plastically at low temperatures (which is not the case for Si and TiW) attention has to be drawn to stay in the elastic regime.
Extending the system to three layers leads to the system in 2.4.3 with the extension of residual stresses in layer 3:

$$\sigma_{xx,1}(z) = E_1 \left[\left(z - {}^{h_1}\!/\!{}_2\right) \kappa + \epsilon_1 \right] \tag{A.5a}$$

$$\sigma_{xx,2}(z) = E_2 \left[\left(z - \left(h_1 + {}^{h_2}\!/\!{}_2\right)\right) \kappa + \epsilon_2 \right] + \sigma_{r,2} \tag{A.5b}$$

$$\sigma_{xx,3}(z) = E_3 \left[\left(z - \left(h_1 + h_2 + {}^{h_3}\!/\!{}_2\right)\right) \kappa + \epsilon_3 \right] + \sigma_{r,3} \tag{A.5c}$$

Again, strain has to be continuous.

$$\epsilon_{xx,1}(z = h_1) = \epsilon_{xx,2}(z = h_1) \tag{A.6a}$$

$$\epsilon_{xx,2}(z = h_1 + h_2) = \epsilon_{xx,3}(z = h_1 + h_2) \tag{A.6b}$$

with

$$\epsilon_{xx,1}(z) = \left(z - {}^{h_1}\!/\!{}_2\right) \kappa + \epsilon_1 + \alpha_1 \Delta T \tag{A.7a}$$

$$\epsilon_{xx,2}(z) = \left(z - \left(h_1 + {}^{h_2}\!/\!{}_2\right)\right) \kappa + \epsilon_2 + \alpha_2 \Delta T \tag{A.7b}$$

$$\epsilon_{xx,3}(z) = \left(z - \left(h_1 + h_2 + {}^{h_3}\!/\!{}_2\right)\right) \kappa + \epsilon_3 + \alpha_3 \Delta T \tag{A.7c}$$

and the sum of forces is equal to zero:

$$\Sigma F = 0 = E_1 h_1 \epsilon_1 + h_2 \left(E_2 \epsilon_2 + \sigma_{r,2}\right) + h_3 \left(E_3 \epsilon_3 + \sigma_{r,3}\right) \tag{A.8}$$

Now the residual stress in layer three can be determined by iteration. When measuring the initial curvatures, or curvatures at small temperatures (elastic regime), of both beams one can derive the residual stresses of both layers in one experiment.
These residual stresses can simply be added to the equation system in chapter 2.4.3 in the same way as the TiW residual stresses are incorporated.

B. Internal stress plots

In the following (figures B.1 to B.5) the remaining internal stress plots derived with the analytical model and the FEA analysis are shown. It was described in chapter 5.3.3 that the analytical model was not able to produce any results for sample CuTiW-VB. In that very chapter the main trends, which are also evident in the other samples, of the two models are compared.

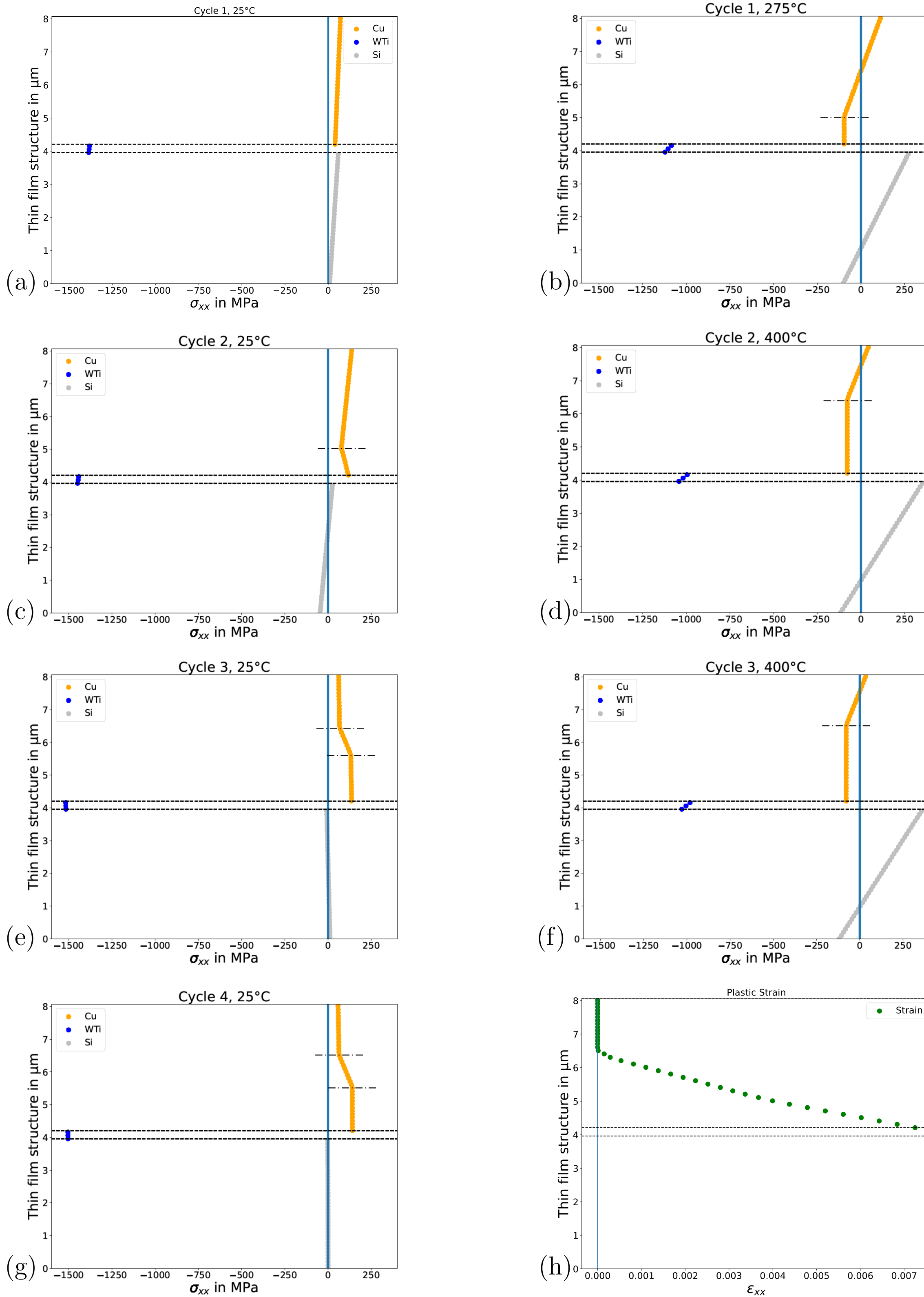

Figure B.1.: Analytical model of CuTiW. Rows correspond to the cycles and columns to low temperature and maximum temperature. In (h) the total accumulated plastic strain after all cycles is shown. The dash dotted lines divide the elastic (top) region, the region plastically deformed below maximum residual stress (middle) and the region deformed to maximum residual stress (bottom) in case of the low temperatures, in case of high temperatures it divides elastic (top) and plastic (bottom) regions.

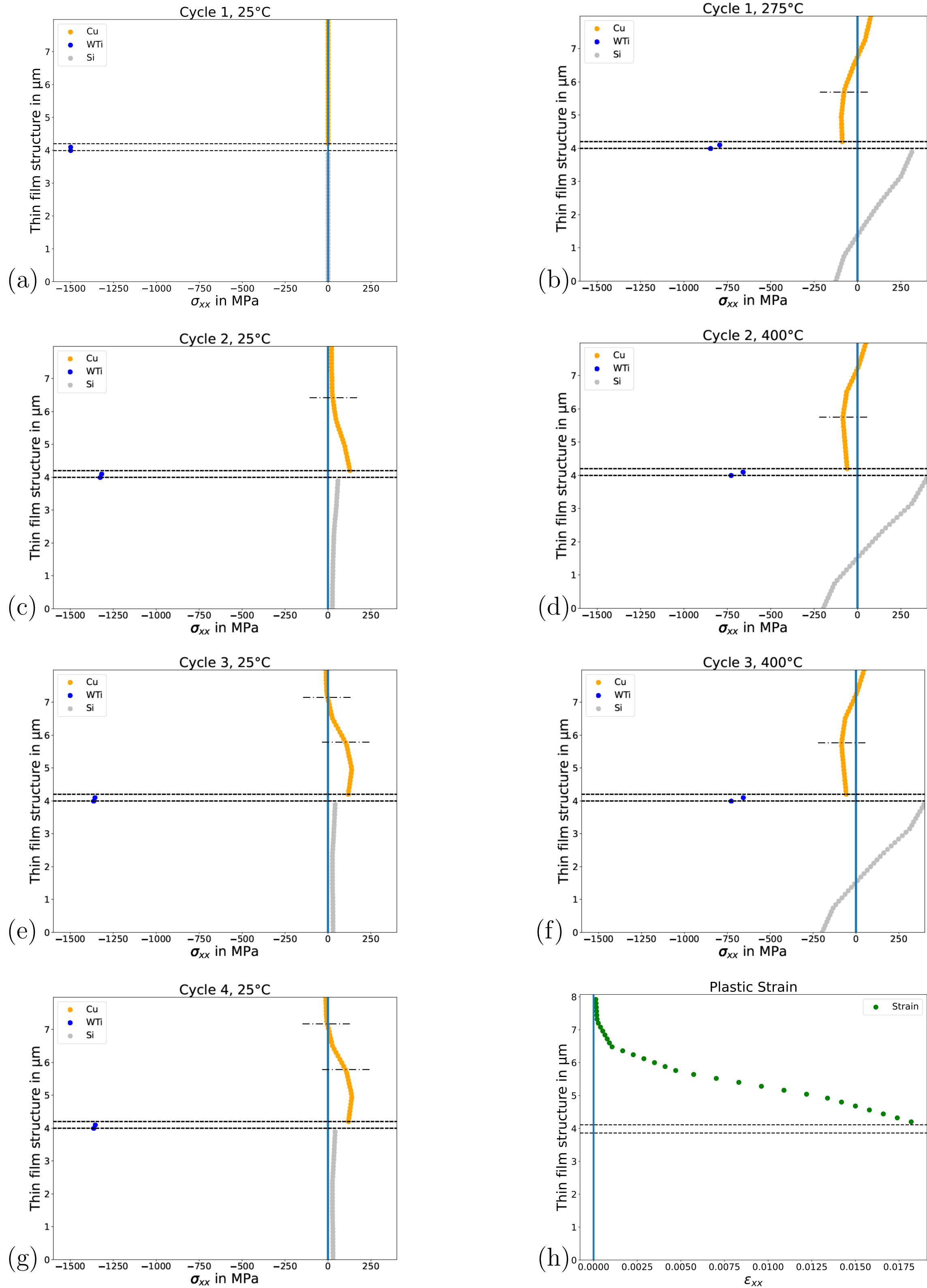

Figure B.2.: FEA model of CuTiW. Rows correspond to the cycles and columns to low temperature and maximum temperature. In (h) the total accumulated plastic strain after all cycles is shown. The dash dotted lines divide the elastic (top) region, the region plastically deformed below maximum residual stress (middle) and the region deformed to maximum residual stress (bottom) in case of the low temperatures, in case of high temperatures it divides elastic (top) and plastic (bottom) regions.

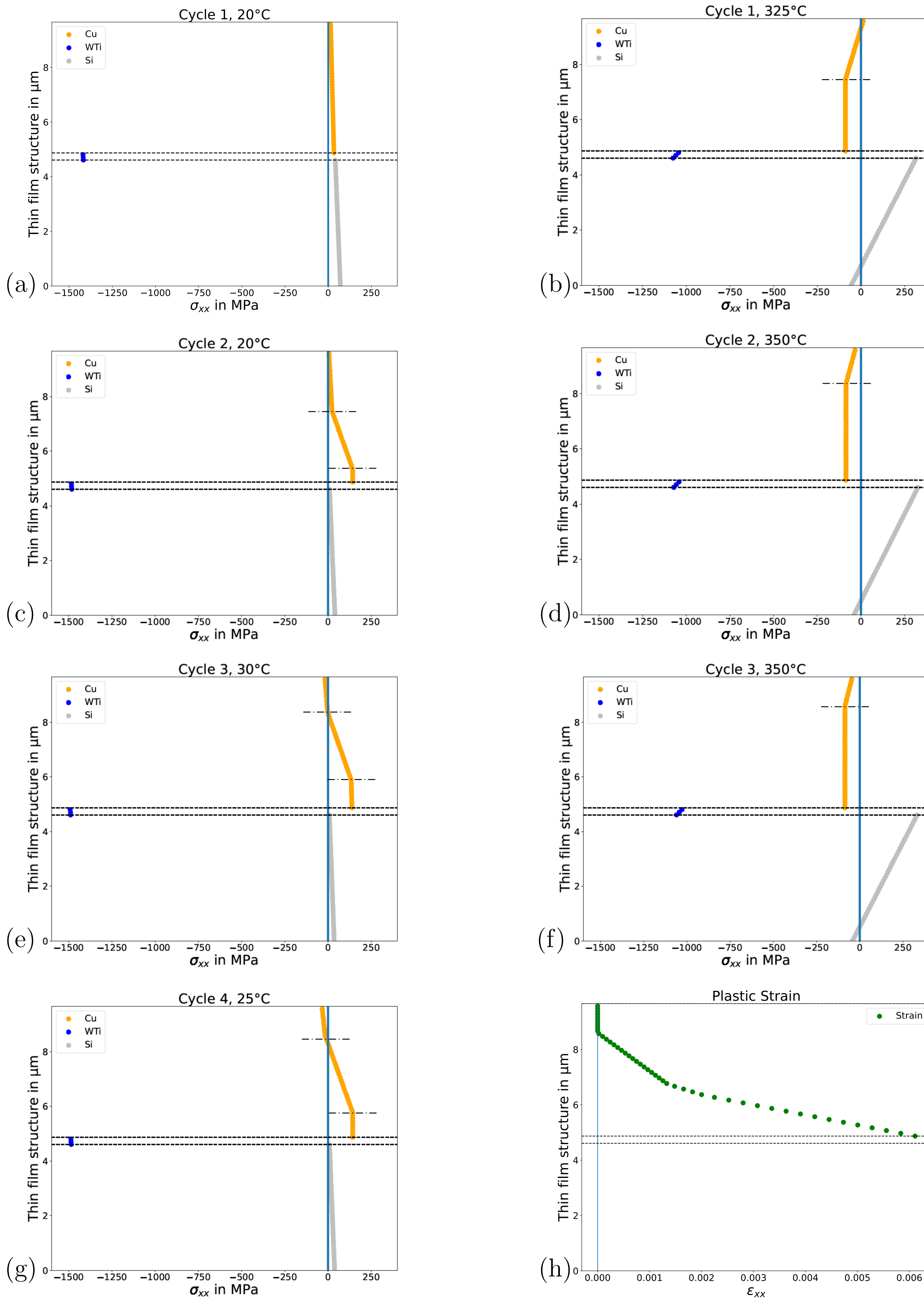

Figure B.3.: Analytical model of CuTiW-Notch. Rows correspond to the cycles and columns to low temperature and maximum temperature. In (h) the total accumulated plastic strain after all cycles is shown. The dash dotted lines divide the elastic (top) region, the region plastically deformed below maximum residual stress (middle) and the region deformed to maximum residual stress (bottom) in case of the low temperatures, in case of high temperatures it divides elastic (top) and plastic (bottom) regions.

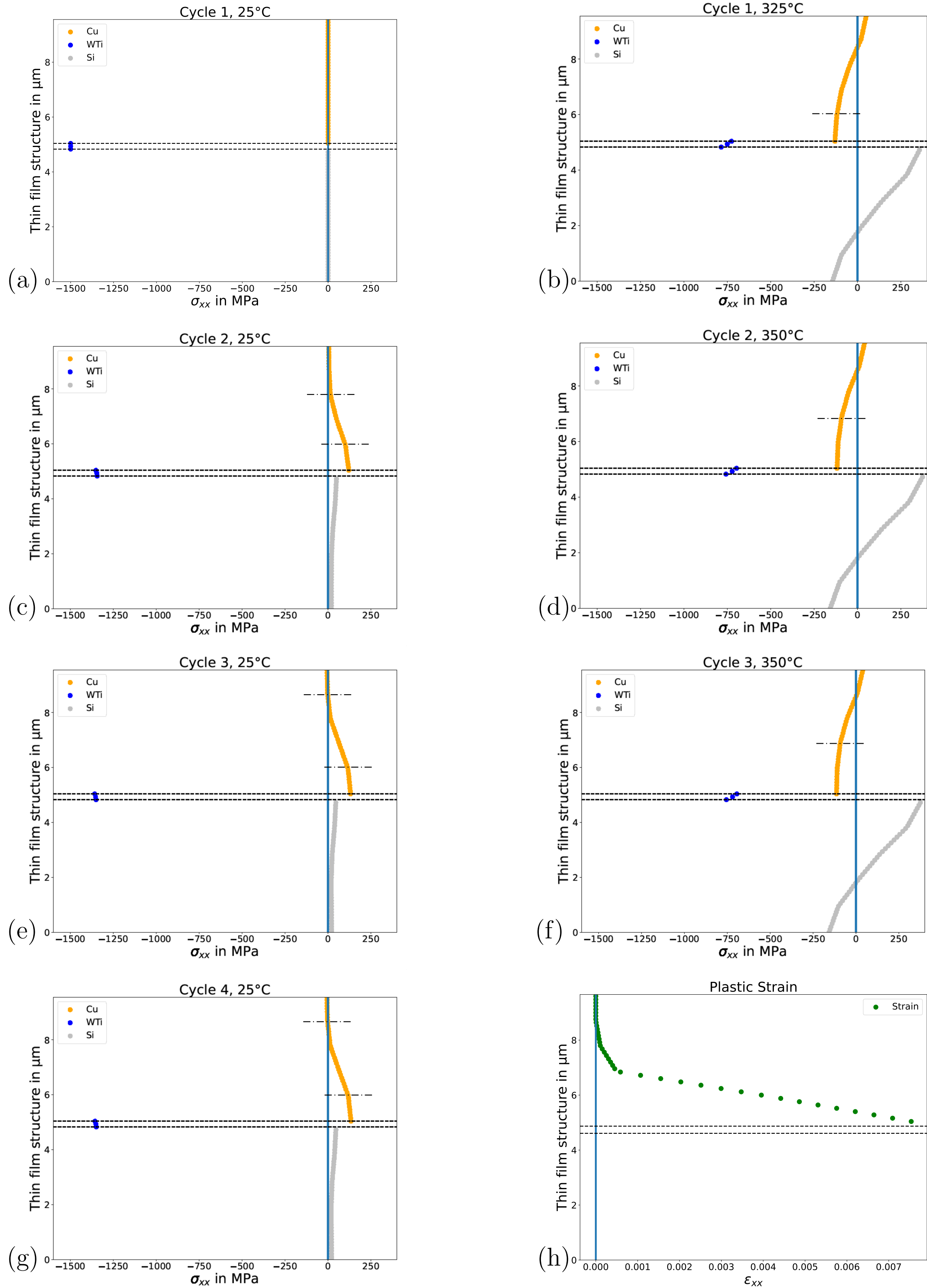

Figure B.4.: FEA model of CuTiW-Notch. Rows correspond to the cycles and columns to low temperature and maximum temperature. In (h) the total accumulated plastic strain after all cycles is shown. The dash dotted lines divide the elastic (top) region, the region plastically deformed below maximum residual stress (middle) and the region deformed to maximum residual stress (bottom) in case of the low temperatures, in case of high temperatures it divides elastic (top) and plastic (bottom) regions.

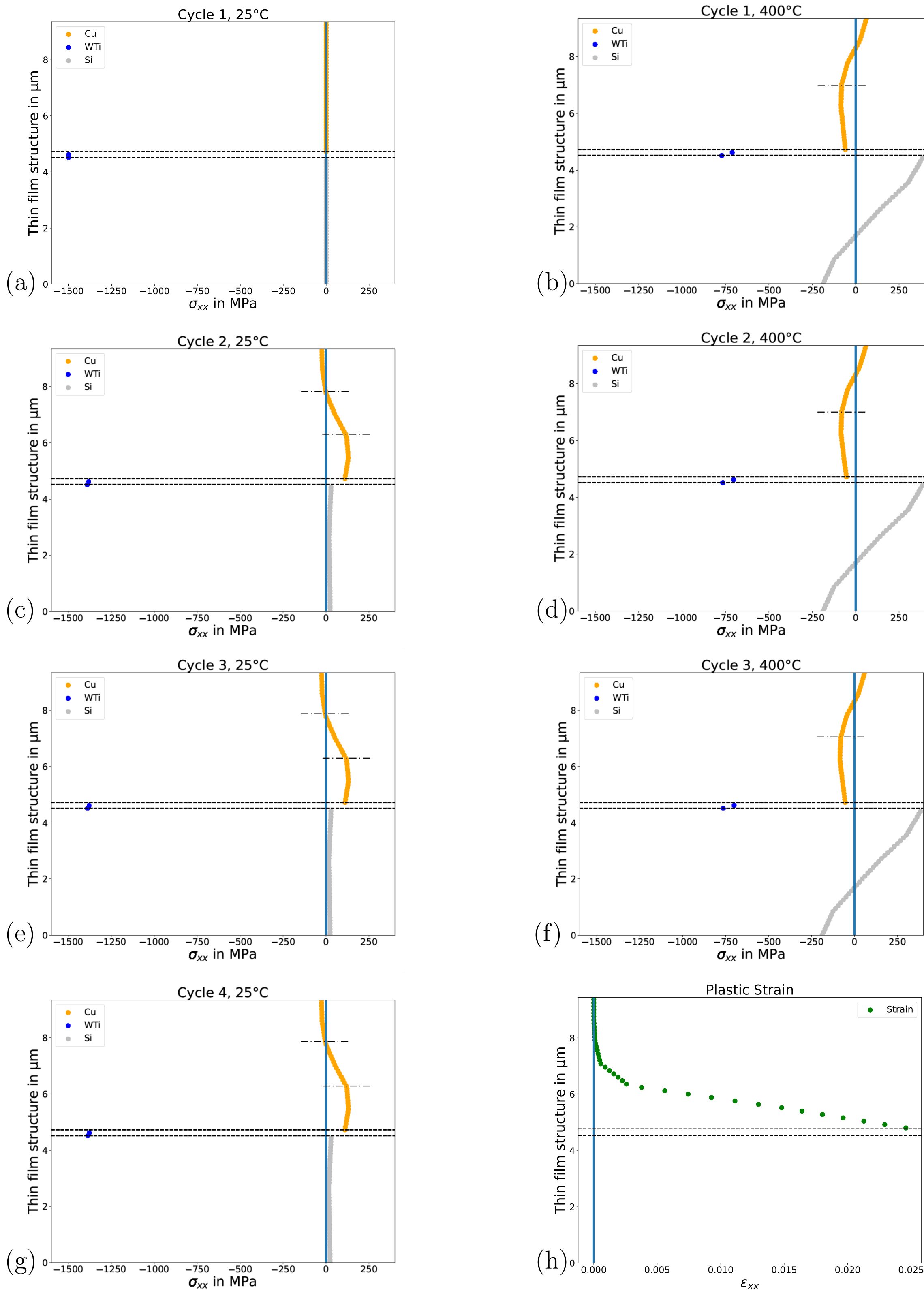

Figure B.5.: FEA model of CuTiW-VB. Rows correspond to the cycles and columns to low temperature and maximum temperature. In (h) the total accumulated plastic strain after all cycles is shown. The dash dotted lines divide the elastic (top) region, the region plastically deformed below maximum residual stress (middle) and the region deformed to maximum residual stress (bottom) in case of the low temperatures, in case of high temperatures it divides elastic (top) and plastic (bottom) regions.

Bibliography

[1] G. E. Moore. "Cramming more components onto integrated circuits". In: *Electronics* 38.8 (1965).

[2] G. E. Moore. "Progress In Digital Integrated Electronics". In: *IEEE Text Speech* (1975).

[3] Grygoriy Kravchenko et al. "Finite element analysis of fatigue cracks formation in power metallisation of a semiconductor device subjected to active cycling". In: *2013 14th International Conference on Thermal, Mechanical and Multi-Physics Simulation and Experiments in Microelectronics and Microsystems (EuroSimE)*. IEEE. 2013, pp. 1–6.

[4] J.O. Olowolafe, C.J. Mogab, and R.B. Gregory. "Evaluation of Ta, Ti and TiW encapsulations for corrosion and diffusion protection of Cu interconnects". In: *Thin Solid Films* 227.1 (1993), pp. 37–43.

[5] M. Fugger et al. "Comparison of WTi and WTi(N) as diffusion barriers for Al and Cu metallization on Si with respect to thermal stability and diffusion behavior of Ti". In: *Microelectronics Reliability* 54.11 (2014), pp. 2487–2493.

[6] J. L. Liotard et al. "Intermetallic compound formations in titanium-copper thin-film couples". In: *Journal of Applied Physics* 57.6 (1985), pp. 1895–1900.

[7] Curran Kalha et al. "Thermal and oxidation stability of Ti x W1- x diffusion barriers investigated by soft and hard x-ray photoelectron spectroscopy". In: *Journal of Applied Physics* 129.19 (2021), p. 195302.

[8] R Rosenberg et al. "Copper metallization for high performance silicon technology". In: *Annual review of materials science* 30.1 (2000), pp. 229–262.

[9] G. Gottstein. *Materialwissenschaft und Werkstofftechnik*. German. 4th Edition. 2014. ISBN: 9783642366024.

[10] Hongliang Chen et al. "Interface Engineering in Organic Field-Effect Transistors: Principles, Applications, and Perspectives". In: *Chemical Reviews* 120.5 (2020), pp. 2879–2949.

[11] Ming Zhou and Shaojun Dong. “Bioelectrochemical Interface Engineering: Toward the Fabrication of Electrochemical Biosensors, Biofuel Cells, and Self-Powered Logic Biosensors”. In: *Accounts of Chemical Research* 44.11 (2011), pp. 1232–1243.

[12] I.P. Jain and Garima Agarwal. “Ion beam induced surface and interface engineering”. In: *Surface Science Reports* 66.3 (2011), pp. 77–172.

[13] Bei Jiang et al. “Interface engineering for two-dimensional semiconductor transistors”. In: *Nano Today* 25 (2019), pp. 122–134.

[14] L. B. Freund and S. Suresh. *Thin Film Materials: Stress, Defect Formation and Surface Evolution*. Cambridge University Press, 2004. ISBN: 9780511754715.

[15] Grégory Abadias et al. “Review Article: Stress in thin films and coatings: Current status, challenges, and prospects”. In: *Journal of Vacuum Science & Technology A* 36.2 (2018), p. 020801.

[16] George Gore and John Tyndall. “X. On the properties of electro-deposited antimony”. In: *Philosophical Transactions of the Royal Society of London* 148 (1858), pp. 185–197.

[17] George Gore and George Gabriel Stokes. “XVII. On the properties of electro-deposited antimony (concluded)”. In: *Philosophical Transactions of the Royal Society of London* 152 (1862), pp. 323–331.

[18] George Gerald Stoney and Charles Algernon Parsons. “The tension of metallic films deposited by electrolysis”. In: *Proceedings of the Royal Society of London. Series A, Containing Papers of a Mathematical and Physical Character* 82.553 (1909), pp. 172–175.

[19] Stephan Bigl et al. “Substrate-Influenced Thermo-Mechanical Fatigue of Copper Metallizations: Limits of Stoney’s Equation”. In: *Materials* 10.11 (2017).

[20] “Introduction”. In: *Cyclic Plasticity of Engineering Materials*. John Wiley & Sons, Ltd, 2017. Chap. 0, pp. 1–12. ISBN: 9781119180838.

[21] “Thermomechanically Coupled Cyclic Plasticity of Metallic Materials at Finite Strain”. In: *Cyclic Plasticity of Engineering Materials*. John Wiley & Sons, Ltd, 2017. Chap. 4, pp. 219–266. ISBN: 9781119180838.

[22] Martin Springer, Michael Nelhiebel, and Heinz E Pettermann. “Fatigue crack growth modeling in the metallization of power semiconductors under cyclic thermo-mechanical loading”. In: *2016 17th International Conference on Thermal, Mechanical and Multi-Physics Simulation and Experiments in Microelectronics and Microsystems (EuroSimE)*. IEEE. 2016, pp. 1–5.

[23] A. Kleinbichler et al. “Annealing effects on the film stress and adhesion of tungsten-titanium barrier layers”. In: *Surface and Coatings Technology* 332 (2017), pp. 376–381.

[24] Rui Huang et al. “Disparate tendency of stress evolution of thin and thick electroplated Cu films at room temperature”. In: *2010 17th IEEE International Symposium on the Physical and Failure Analysis of Integrated Circuits*. 2010, pp. 1–6.

[25] Stephan Bigl et al. “Advanced characterisation of thermo-mechanical fatigue mechanisms of different copper film systems for wafer metallizations”. In: *Thin Solid Films* 612 (2016), pp. 153–164.

[26] Stefan Wurster et al. “Accelerated thermo-mechanical fatigue of copper metallizations studied by pulsed laser heating”. In: *Microelectronic Engineering* 167 (2017), pp. 110–118.

[27] Markus Alfreider, Johannes Zechner, and Daniel Kiener. “Addressing Fracture Properties of Individual Constituents Within a Cu-WTi-SiOx-Si Multilayer”. In: *JOM* 72.12 (2020), pp. 4551–4558.

[28] R. Bodlos et al. “Ab initio investigation of the atomic volume, thermal expansion, and formation energy of WTi solid solutions”. In: *Phys. Rev. Materials* 5.4 (2021), p. 043601.

[29] Markus Alfreider et al. “The influence of chemistry on the interface toughness in a WTi-Cu system”. In: *Acta Materialia* 230 (2022), p. 117813.

[30] Alexander Wimmer et al. “Temperature dependent transition of intragranular plastic to intergranular brittle failure in electrodeposited Cu micro-tensile samples”. In: *Materials Science and Engineering A* 618 (Nov. 2014), pp. 398–405.

[31] Alexander Wimmer et al. “Damage evolution during cyclic tension–tension loading of micron-sized Cu lines”. In: *Acta Materialia* 67 (Apr. 2014), pp. 297–307.

[32] A. Wimmer et al. “Cyclic bending experiments on free-standing Cu micron lines observed by electron backscatter diffraction”. In: *Acta Materialia* 83 (2015), pp. 460–469.

[33] A. Wimmer et al. “Micro-tension study of miniaturized Cu lines at variable temperatures”. In: *Acta Materialia* 92 (2015), pp. 243–254.

[34] Stephan Bigl et al. “Correlative microstructure and topography informed nanoindentation of copper films”. In: *Surface and Coatings Technology* 308 (2016), pp. 404–413.

[35] Sebastian Moser et al. "A Novel Setup for In Situ Monitoring of Thermomechanically Cycled Thin Film Metallizations". In: *JOM* 71.10 (2019), pp. 3399–3406.

[36] Manuel Kleinbichler et al. "Quantitative analysis of void initiation in thermomechanical fatigue of polycrystalline copper films". In: *Microelectronics Reliability* 127 (2021), p. 114387.

[37] Paul Hoffmann et al. "Thermomechanical fatigue damage modeling and material parameter calibration for thin film metallizations". In: *International Journal of Fatigue* 155 (2022), p. 106627.

[38] Georg Kirchgaßner. "In-situ thermal bending of Cu/TiW/Si tri-layer microcantilevers". Bachelor Thesis. Montanuniversität Leoben, 2020.

[39] Mang H. Hoffstetter G. *Festigkeitslehre*. 4th. edition. Springer, 2013. ISBN: 978-3-642-40751-2.

[40] S. Timoshenko. "Analysis of Bi-Metal Thermostats". In: *J. Opt. Soc. Am.* 11.3 (1925), pp. 233–255.

[41] S. N. G. Chu. "Elastic Bending of Semiconductor Wafer Revisited and Comments on Stoney's Equation". In: *Journal of The Electrochemical Society* 145.10 (1998), pp. 3621–3627.

[42] C.H. Hsueh. "Thermal stresses in elastic multilayer systems". In: *Thin Solid Films* 418.2 (2002), pp. 182–188.

[43] Y. Y. Hu and W. M. Huang. "Elastic and elastic-plastic analysis of multilayer thin films:Closed-form solutions". In: *Journal of Applied Physics* 96.8 (2004), pp. 4154–4160.

[44] Manuel J. Pfeifenberger et al. "The use of femtosecond laser ablation as a novel tool for rapid micro-mechanical sample preparation". In: *Materials and Design* 121 (2017), pp. 109–118.

[45] R. Fritz and D. Kiener. "Development and application of a heated in-situ SEM micro-testing device". In: *Measurement* 110 (2017), pp. 356–366.

[46] J. Canny. "A Computational Approach to Edge Detection". In: *IEEE Transactions on Pattern Analysis and Machine Intelligence* PAMI-8.6 (1986), pp. 679–698.

[47] R. Schöngrundner et al. "Critical assessment of the determination of residual stress profiles in thin films by means of the ion beam layer removal method". In: *Thin Solid Films* 564 (2014), pp. 321–330.

[48] Hiroshi Tada, Paul C. Paris, and George R. Irwin. *The Stress Analysis of Cracks Handbook*. 3rd Edition. ASME Press, 2000. ISBN: 0791801535.

[49] Joachim Rösler, Harald Harders, and Martin Bäker. *Mechanisches Verhalten der Werkstoffe*. 6th Edition. Springer, 2003. ISBN: 9783658268015.

[50] B. Beausir and J.-J. Fundenberger. *Analysis Tools for Electron and X-ray diffraction*. 2017. URL: `www.atex-software.eu`.

[51] Yingen Xiong and Kari Pulli. “Fast Panorama Stitching for High-Quality Panoramic Images on Mobile Phones”. In: *Consumer Electronics, IEEE Transactions on* 56 (2010), pp. 298–306.

[52] J. Schindelin et al. “Fiji: an open-source platform for biological-image analysis”. In: *Nature Methods* 9 (2012), pp. 676–682.

[53] Preibisch Stephan, Saalfeld Stephan, and Tomancak Pavel. “Globally optimal stitching of tiled 3D microscopic image acquisitions”. In: *Bioinformatics* 11 (2009), pp. 1463–1465.

[54] Ethan Rublee et al. “ORB: An efficient alternative to SIFT or SURF”. In: *2011 International Conference on Computer Vision*. 2011, pp. 2564–2571.

[55] Richard O. Duda and Peter E. Hart. “Use of the Hough transformation to detect lines and curves in pictures”. In: *Commun. ACM* 15 (1972), pp. 11–15.

[56] Dana H. Ballard. “Generalizing the Hough transform to detect arbitrary shapes”. In: *Pattern Recognition* 13 (1981), pp. 111–122.

[57] Harry Wechsler and Jack Sklansky. “Finding the rib cage in chest radiographs”. In: *Pattern Recognition* 9 (1977), pp. 21–30.

[58] Nick Connor. *Copper - Melting Point*. 2017. URL: `https://www.periodic-table.org/copper-melting-point/` (visited on 05/08/2022).

[59] Yao Jiang et al. “Impurity effect on recrystallization and grain growth in severe plastically deformed copper”. In: *Materials Science and Engineering: A* 824 (2021), p. 141786.

[60] Paul Hoffmann et al. “Simulation of Fatigue Damage in Clusters of DMOS Cells Subjected to Non-Uniform Transient Thermo-Mechnical Loading”. In: 2020, pp. 1–9.

[61] Barbara Pedretscher, Michael Nelhiebel, and Barbara Kaltenbacher. “Applying a Statistical Model to the Observed Texture Evolution of Fatigued Metal Films”. In: *IEEE Transactions on Device and Materials Reliability* 20.3 (2020), pp. 517–523.

[62] Curran Kalha et al. *Evaluation of the Thermal Stability of TiW/Cu Heterojunctions Using a Combined SXPS and HAXPES Approach.* 2022.

[63] S. Chen et al. "An ion beam layer removal method of determining the residual stress in the as-fabricated TSV-Cu/TiW/SiO2/Si interface on a nanoscale". In: *Microelectronics Reliability* 112 (2020), p. 113826.

[64] S. Massl et al. "Stress measurement in thin films with the ion beam layer removal method: Influence of experimental errors and parameters". In: *Thin Solid Films* 516.23 (2008), pp. 8655–8662.

[65] E. Kirkendall, C. Upthegrove, and L. Thomassen. "Rates of Diffusion of Copper and Zinc in Alpha Brass". In: *American Institute of mining and metallurgical engineers* 133 (1938), pp. 186–203.

[66] M.F. Ashby. *Materials Selection in Mechanical Design.* 4th Edition. Knovel Library. Butterworth-Heinemann, 1999. ISBN: 9780750643573.